REVIEW ARTICLE

Planetary cloud tracking

Tianshu Liu[1] · David M. Salazar[1]

Abstract

From a perspective of experimental fluid mechanics, this review describes cloud-tracking methods to extract high-resolution velocity fields from publically available images of planets (such as Jupiter, Saturn and Earth) obtained from ground-based and space-based observations. These methods include manual tracking, correlation image velocimetry (CIV) and optical flow method (OFM) that have been applied to various images of planets. The relevant issues such as image navigation, image registration and metric conversion are also discussed. The accuracy of the open-source cloud-tracking algorithms is evaluated based on simulated cloud images of Jupiter's Great Red Spot (GRS). As an example, the application of cloud tracking to the GRS cloud images obtained from NASA's space flight missions is discussed, progressively revealing the complex flow structures of the GRS. Although the cloud images of Jupiter and Saturn are mainly used in this paper, the cloud tracking methods are also applicable to satellite cloud images of Earth. As an extra example, OFM is applied to the satellite infrared images of Typhoon Rai to extract the flow structure of Rai's top layer. This review tries to open a window for experimental fluid dynamicists to explore intriguing planetary flows based on cloud images of planets.

Graphical abstract

(a)   (b)
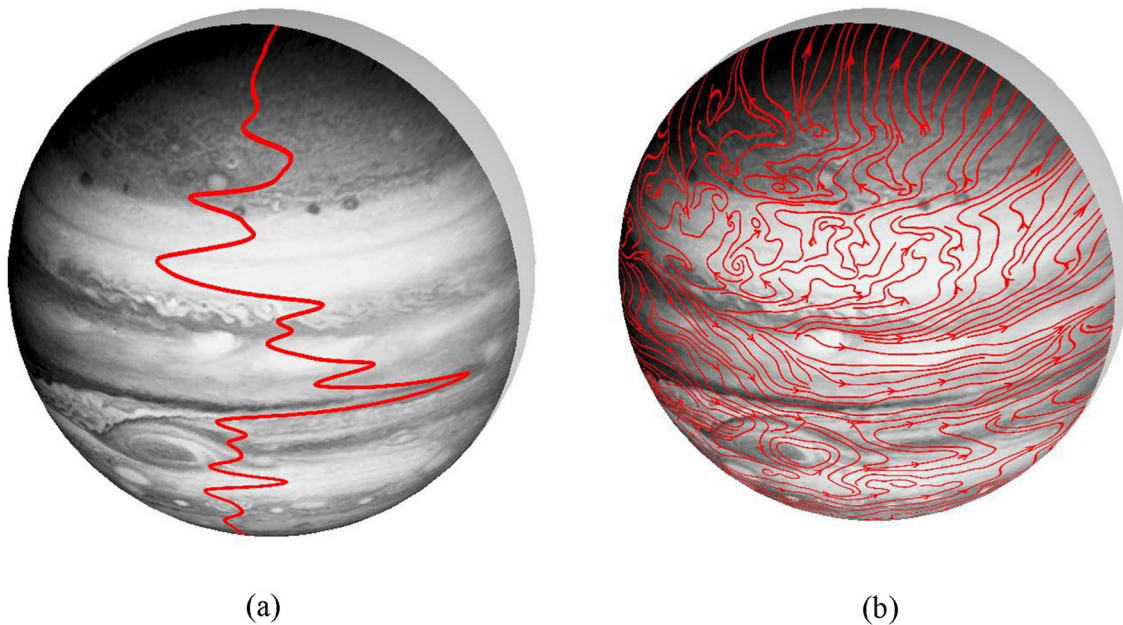
✉ Tianshu Liu
    tianshu.liu@wmich.edu

[1]   Department of Mechanical and Aerospace Engineering,
      Western Michigan University, Kalamazoo, MI 49008, USA

1 Introduction

The atmospheres of planets (including Jupiter, Saturn and Earth) with dense atmospheres have dynamic flow structures visualized by their clouds, which play important roles in physical processes related to heat flux, temperature, pressure, composition, and radiation (Dowling 1995; Ingersoll et al. 2004; Ingersoll 2020). A vivid example can be seen in Fig. 1, which was constructed from images taken by the narrow angle camera onboard NASA's Cassini spacecraft on December 29, 2000, during its closest approach to the giant planet at a distance of approximately 10 million kilometers (PIA04866 at https://photojournal.jpl.nasa.gov/). In this mosaic image of the colorful clouds of Jupiter, the light and dark bands (the zones and belts) associated with jet streams are observed. The Great Red Spot (GRS) and White Ovals (WOs) are also observed between two opposite jet streams. The GRS is at least 150 years old (may be older) since Hooke (1665) reported an observed dark spot on Jupiter that may be the GRS. A review of the historical and contemporary observations of the GRS was given by Simon et al. (2018). It is observed that the GRS shrank by 15% from 1996 to 2006, both in terms of its visible appearance and its ring of circumferential winds. South of the GRS, lies a zone of anticyclonic vorticity where large white oval-shaped (WO) vortices are
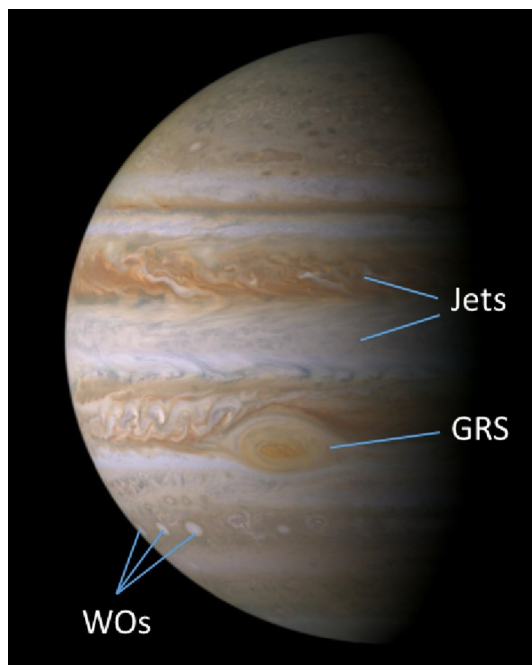
commonly observed. One such vortex, Oval BA formed as a result of the mergers of three other WOs (namely Ovals DE, FA, and BC) in the 1990s (Choi et al. 2010). These vortices are anticyclones with circumferential winds greater than 100 m/s, drifting slowly in longitude but staying fixed in latitude (Asay-Davis et al. 2009; Choi et al. 2010). In a certain sense, Jupiter can be considered as a natural fluid dynamics laboratory, where rich and complex flow structures like eddies, vortices, jets and waves at very high Reynolds numbers can be studied. More Jupiter's images and images of other planets obtained in various NASA space flight missions are available at https://photojournal.jpl.nasa.gov/.

Because clouds provide passive tracers of winds, cloud tracking has been the primary method of measuring wind speeds in planetary atmospheres through Earth- and space-based remote sensing. Cloud-tracking wind measurements are important goals in NASA space flight missions including Voyager, Galileo, Cassini, and New Horizons. However, imaging of the giant planets typically give images with a low physical spatial resolution (several to hundred km/pixel) with a larger sampling interval (typically 40 min to 10 h), which is constrained by some factors such as fast planetary rotation, data volume limitation, and pointing stability. Challenges remain in cases where a spacecraft is in close proximity to a planet. In particular, because of the motion of the spacecraft relative to the planet and sun, the illumination level can change dramatically between consecutive images. The effect of the illumination level should be corrected in cloud tracking. Unlike satellite-based cloud-tracking measurements on Earth, the planetary measurements cannot easily be verified against in-situ data. Therefore, it is highly desirable to develop the robust cloud-tracking methods under the above severe constraints. Various methods have been developed by researchers in planetary sciences to deduce winds from the motion of trackable cloud features after planetary mission-based imaging science campaigns began.

Manual tracking is the simplest method that works by visually inspecting a sequence of cloud maps, identifying common cloud features in sequence and marking their coordinates. This method has been used in determining long-term trends in zonal winds of Jupiter using Voyager, Hubble Space Telescope (HST), Galileo and Cassini data (Mitchell et al. 1981; Limaye 1986; Dowling and Ingersoll 1988; Sada et al. 1996; Vasavada et al. 1998; Simon-Miller et al. 2002, 2006, 2007; Simon-Miller and Gierasch 2010; Sánchez-Lavega et al. 2000; Cheng et al. 2008). The simplest automated cloud tracking method is the one-dimensional (1D) correlation method, which works for images with a relatively poor contrast and limited viewed region to measure only the zonal-mean zonal-wind profile. This method has been used

Fig. 1 The high-resolution, full-disk color mosaic of Jupiter. The mosaic was assembled from over 30 individual images, allowing for the planet's rotation as the images were taken (PIA04866 at https://photojournal.jpl.nasa.gov/)

by Limaye (1986), Garcia-Melendo and Lanchez-Lavega (2001), Sayanagi et al. (2019), and Johnson et al. (2018).

Correlation imaging velocimetry (CIV) is an automated method that produces wind velocity vectors from a pair of mapped images by calculating the displacements in interrogation windows using the two-dimensional (2D) cross-correlation method (Tokumaru and Dimotakis 1995; Choi et al. 2009, 2010; Kouyama et al. 2012; Hueso et al. 2009; Sussman et al. 2010). CIV has been used to derive wind fields on Venus using Galileo and Venus Express images (Kouyama et al 2012, 2013), Jupiter's GRS using Galileo images (Choi et al. 2007), Oval BA using Galileo, Cassini and New Horizon images (Hueso et al. 2009; Choi et al. 2010), and Saturn using Cassini images (Sayanagi et al. 2011). An improved CIV is the Advection Corrected Correlation Imaging Velocimetry (ACCIV) method developed by Asay-Davis et al. (2009), in which an advection-corrected scheme tracking feature trajectories in a time sequence of images is incorporated. ACCIV has been used to obtain high-resolution wind fields of the GRS and Oval BA (Asay-Davis et al. 2009).

The optical flow method (OFM) is suitable for extraction of velocity vectors from cloud images at a spatial resolution of one vector per a pixel (Liu and Shen 2008; Heitz et al. 2010; Liu et al. 2015). OFM has been used to study the structures of the GRS (Liu et al. 2012a, b) and Saturn's north polar vortex (Liu et al. 2019). OFM is developed by projecting the transport equation of scalar tracers in the 3D object space onto the 2D image plane (Liu and Shen 2008). Thus, this 3D partial differential equation (PDE) is reduced to a 2D PDE called the optical flow equation in the image plane, where the physical meaning and mathematical definition of the optical flow are elucidated. In contrast to the correlation-based method in CIV (or PIV), the variational OFM is a differential method that seeks a numerical solution to the Euler–Lagrange equation to determine displacement vectors between a pair of cloud images.

Before applying the cloud tracking methods, planetary cloud images (or maps) should be processed since they are obtained by an imaging system (camera) onboard a moving spacecraft relative to a rotating planet. Since two consecutive images with a large time interval are usually misaligned due to the motion of the onboard camera relative the planet, image navigation/image registration is required (Hueso et al. 2010). After image navigation/image registration, cloud images at different times are aligned such that the cloud tracking methods could be used to extract fluid velocity fields. Furthermore, in a large time interval between two consecutive images, the illuminating angle of sunlight with respect to the planet surface and the viewing angle of a camera could change, leading to a local variation of the illumination intensity. Therefore, this local illumination variation should be corrected.

In the atmosphere of Earth that is a unique environment for humankind, there are also distinct dynamic large-scale flow structures particularly hurricanes in Atlantic Ocean and Northeast Pacific Ocean, typhoons in Northwest Pacific Ocean, and cyclones in South Pacific Ocean and Indian Ocean. Although hurricanes (representing typhoons and cyclones also) are encountered and observed every year, the prediction of the formation, maintenance and motion of hurricane remains a difficult problem in fluid mechanics since rotating stratified flow dynamics, boundary layers, convection, and air-sea interaction are complicatedly involved in hurricanes (Emanuel 1991; Smith and Vogl 2003). Velocity measurements in hurricanes provide not only timely knowledge of storm's intensity, trajectory and anticipated lifetime, but also necessary data to understand the structures of hurricanes (Merrill 1988). Velocity measurement methods include ground-based and airborne Doppler radar (Tuttle and Gall 1999), airborne Doppler Lidar (Bucci et al. 2018), airborne Stepped-Frequency Microwave Radiometer (Uhlhorn and Black 2003), satellite microwave radiometers (Meissner et al. 2021), and reconnaissance aircraft passing through the storm (Willoughby et al. 1982). Since time sequences of cloud images are obtained by geostationary environmental and weather satellites, cloud tracking has been developed as a useful tool to determine atmospheric flows on Earth (Leese et al. 1971; Ottenbacher et al. 1997; Menzel 2001). Héas et al. (2007) and Héas and Mémin (2008) developed OFM by incorporating some physical constraints for motion estimation of atmospheric flows on Earth from satellite images. Based on the continuity equation with a variable density, they gave the optical flow equations for cloud layers at different altitudes in the atmosphere and then proposed the variational formulations for estimation of the horizontal velocities and vertical velocity in the layers. Satellite images of hurricanes, typhoons and cyclones are available in the website of Marine Meteorology Division of Ocean and Atmospheric Science and Technology Directorate in US Naval Research Laboratory (NRL) (https://www.nrlmry.navy.mil/tcdat/tc2021/). Since geostationary satellites constantly observe the specific regions of interest on Earth, time sequences of high-resolution cloud images are ready for cloud tracking without some problems encountered in observations by spacecraft orbiting other planets such as image navigation, image registration, low physical spatial resolution, and large time interval between two sequential images. In addition, cloud tracking on Earth can be calibrated and validated based on ground-based velocity measurements, which is not possible on other planets. From this perspective, the planetary cloud-tracking methods described in this paper are readily and favorably applicable to Earth.

Essentially, planetary cloud tracking is a topic of determining velocity fields from natural flow visualization images (cloud images) on planets. The objective of this

review is to provide an introduction of planetary cloud tracking to researchers in experimental fluid mechanics. First, some relevant aspects of planetary cloud tracking are discussed, including image navigation, image registration, and metric conversion from images onto a planetary surface. Then, manual tracking and CIV are briefly described and their application to Jupiter's GRS images is discussed. Next, the working principle of OFM for cloud tracking is described, including the optical flow equation and its variational solution. Based on simulated cloud images of the GRS, several cloud-tracking algorithms are evaluated, indicating that OFM is particularly suitable to planetary cloud tracking. Broadly speaking, OFM can be used to measure fluid motions in natural or less-controlled environments in which particulate tracers are dispersed. In an example of the application of OFM, the high-resolution velocity field extracted from a pair of the Galileo 1996 images of the GRS is presented and the flow structures of the GRS including the elliptical high-speed collar and the complex inner region are analyzed. In another example, the velocity fields of the developing Typhoon Rai are extracted from a time sequence of satellite infrared images.

2 Relevant aspects on processing planetary images

2.1 Image navigation

Cloud tracking is carried out on images of the atmospheres of the planets taken by spacecraft orbiting around them. The extracted velocity data should be mapped onto a planetary surface (an ellipsoidal surface). The navigation of planetary images is the mathematical process that assigns the longitude and latitude coordinates to each pixel on the image plane. The image navigation is the first step for cloud tracking to align cloud images obtained by a moving spacecraft relative a rotating planet. Furthermore, it is required to map velocity fields extracted on the image plane onto a planetary surface.

As shown in Fig. 2, a point above an ellipsoid is either expressed in the Cartesian coordinates (X, Y, Z) or in the curvilinear coordinates (ϕ, λ, h) that are the geodetic latitude, longitude and ellipsoidal height in the meteorological conventions (Holton and Hakim 2013). In the planetary sciences, ϕ is considered as the planetographic latitude ϕ_g. In the Cartesian coordinate system, the Z-axis coincides with the position of the rotation axis. The X-axis is suitably assigned on the equator, and the Y-axis completes a right-handed coordinate system by passing through the intersection of the 90° E meridian and the equator. The
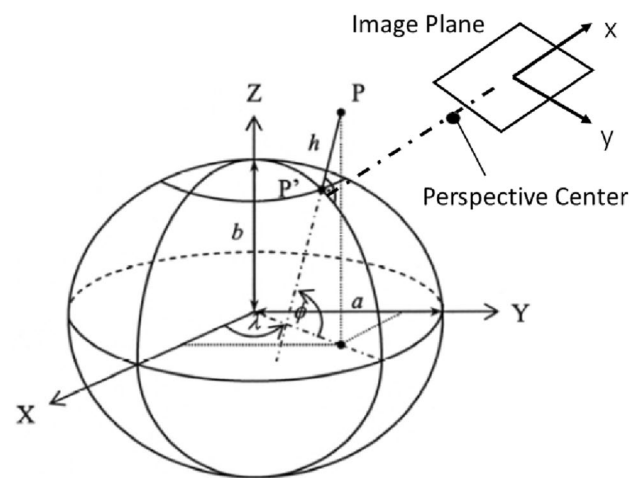

Fig. 2 The ellipsoidal coordinate system and the image plane. Adapted from Janssen (2009)

relation between the Cartesian coordinates and the curvilinear coordinates is given by Janssen (2009)

$$\begin{bmatrix} X \\ Y \\ Z \end{bmatrix} = \begin{bmatrix} (\nu + h) \cos \phi \cos \lambda \\ (\nu + h) \cos \phi \sin \lambda \\ \left(\nu\left(1 - e^2\right) + h\right) \sin \phi \end{bmatrix} \equiv g(\phi, \lambda, h), \tag{1}$$

where ν represents the radius of curvature in the prime vertical defined as

$$\nu = \frac{a}{\sqrt{1 - e^2 \sin^2 \phi}}. \tag{2}$$

In Eq. (1), $e = \sqrt{2f - f^2}$ is the first eccentricity of the ellipsoid, $f = (a - b)/a$ is the flattening, and a and b are the lengths of the semi-major axis and semi-minor axis of the planet (the equatorial and polar radii denoted by R_e and R_p also), respectively. On the ellipsoid with $h = 0$, the surface Cartesian coordinates (X, Y, Z) are a function of the surface curvilinear coordinates (ϕ, λ), i.e., $(X, Y, Z) = g(\phi, \lambda, 0)$. The inverse conversion can be iteratively made using the following relations (Torge 2001),

$$\phi = \tan^{-1} \left[\frac{Z}{\sqrt{X^2 + Y^2}} \left(1 - e^2 \left(\frac{\nu}{\nu + h}\right)\right)^{-1} \right], \tag{3a}$$

$$\lambda = \tan^{-1} \left[Y/X\right], \tag{3b}$$

$$h = \sqrt{X^2 + Y^2} \sec \phi - \nu. \tag{3c}$$

Figure 2 shows the perspective projection relationship between a point (X, Y, Z) in the object space and the

corresponding point (x, y) in the image plane. The perspective projection is illustrated in Fig. 2 as the dashed line connecting a point on the surface and a point on the image through the perspective center. The lens of a camera is modeled by a single point known as the perspective center denoted by $(X_c, \ Y_c, \ Z_c)$ in the object space. The collinearity equations relating (x, y) to (X, Y, Z) are symbolically given by Liu et al. (2012a, b)

$$(x, \ y) = f(X, Y, Z; \Pi_{ex}, \Pi_{in}). \tag{4}$$

In Eq. (4), the exterior orientation parameter set Π_{ex} contains the Euler angles $(\omega, \ \varphi, \ \kappa)$ defining the orientation of a camera and the perspective center position $(X_c, \ Y_c, \ Z_c)$ defining the camera position. For a moving camera in flight, the exterior orientation parameters are functions of time. The interior orientation parameter set Π_{in} contains the principal distance c, the principal-point location $(x_p, \ y_p)$ and the lens distortion parameters (K_1, K_2, P_1, P_2). The interior orientation parameters are usually fixed in flight.

Analytical camera calibration/orientation techniques can be used to solve the collinearity equations for the determination of the interior and exterior orientation parameters of a camera system (Liu et al. 2012a, b). The interior orientation parameters of a camera can be determined on the ground in a laboratory, and it is assumed that these pre-determined parameters are fixed in flight. Sometimes, these parameters (and additional higher-order distortion parameters) are refined using in-flight calibration data. To determine the exterior orientation parameters, at least three fiducial marks with known coordinates on the planetary surface are required. In the following example of Jupiter, the north pole, the mid-point and edge-point of the equator, and the center of the GRS in images are used as the fiducial marks. In addition, the planet limb arc could be used as an additional constraint. The known flight data (orbit and orientation) of a spacecraft can be used for initial estimation of the exterior orientation parameters. When the exterior and interior orientation parameters are known, the one-to-one mapping between the planetary surface curvilinear coordinates $(\phi, \ \lambda)$ and the image coordinates (x, y) is given by

$$(x, \ y) = f(g(\phi, \lambda, 0); \Pi_{ex}, \Pi_{in}). \tag{5}$$

Specialized software such as The Planetary Laboratory for Image Analysis (PLIA) is developed for image navigation and processing in planetary sciences (Hueso et al. 2010). Integrated Software for Imagers and Spectrometers (ISIS) is also a useful digital image processing software package to manipulate imagery collected by NASA and International planetary missions in the Solar System (https://isis.astro geology.usgs.gov/index.html).

The original Voyager "Blue Movie" (PIA02855 at https://photojournal.jpl.nasa.gov/) is considered as an example, recording the approach of Voyager 1 during a period of over 60 Jupiter days in 1979. This sequence is made from 66 images taken once every Jupiter rotation period (about 10 h). These images were acquired in the blue filter from January 6 to February 3, 1979. The spacecraft flew from 58 million kilometers to 31 million kilometers from Jupiter during that time. The images are re-scaled and rotated for image navigation/registration
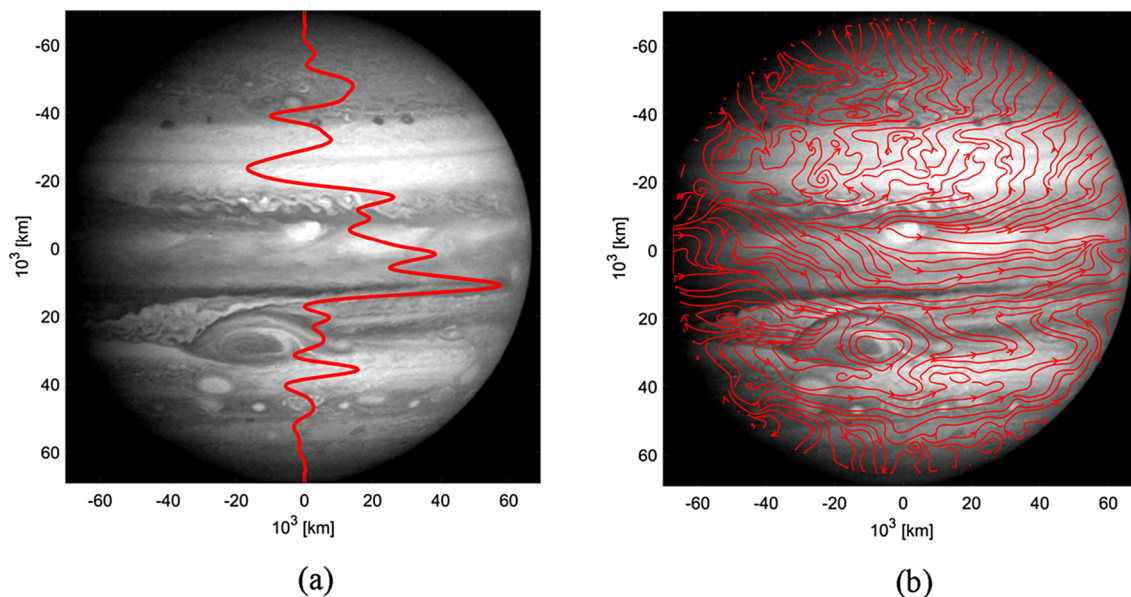

Fig. 3 **a** Typical image of Jupiter taken by Voyager 1 with the time-averaged zonal velocity profile, and **b** time-averaged streamlines in the image

by matching the planet limb arc before applying OFM to the images to extract high-resolution velocity fields. A sequence of 65 snapshot velocity fields is obtained. Figure 3a shows a typical image of Jupiter superposed with the time-averaged zonal velocity profile. Figure 3b shows time-averaged streamlines in the image extracted using OFM, indicating the complexity of the global flow field on Jupiter. The interaction of the zonal jet streams and storms

shows how dynamic the Jovian atmosphere is. The results on the image plane in Fig. 3 are mapped onto the Jupiter ellipsoidal surface, as shown in Fig. 4.

2.2 Image registration

Typically, a sequence of planetary cloud images is captured by a camera onboard spacecraft with a large time interval

(a)   (b)
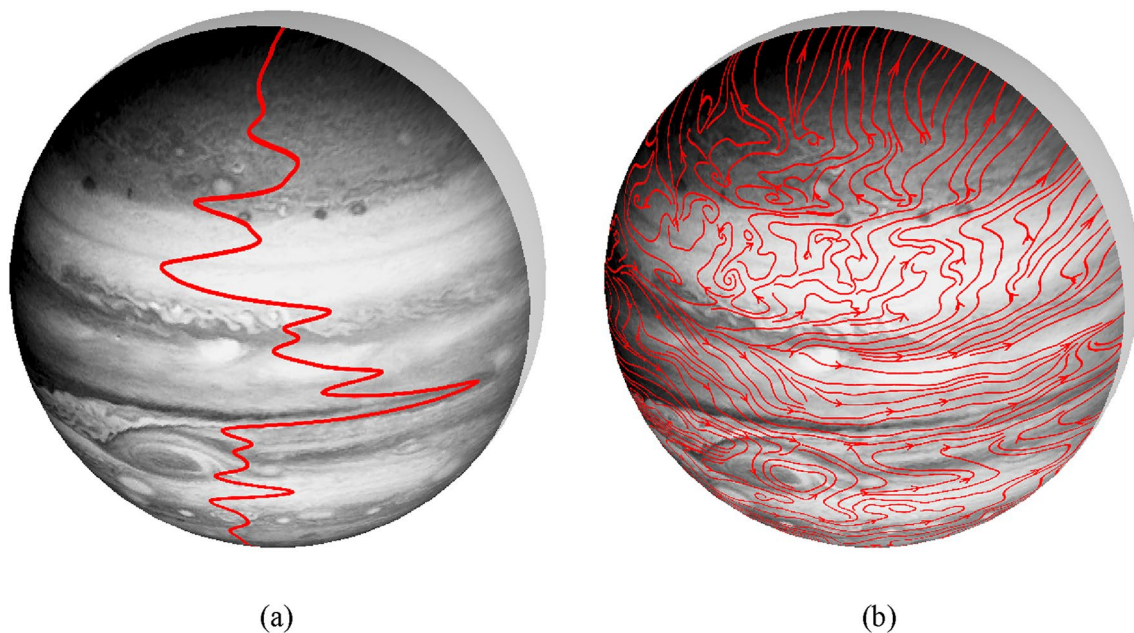
Fig. 4 a Typical cloud pattern mapped onto the Jupiter surface superposed with the time-averaged zonal velocity profile, and **b** streamlines mapped onto the Jupiter surface
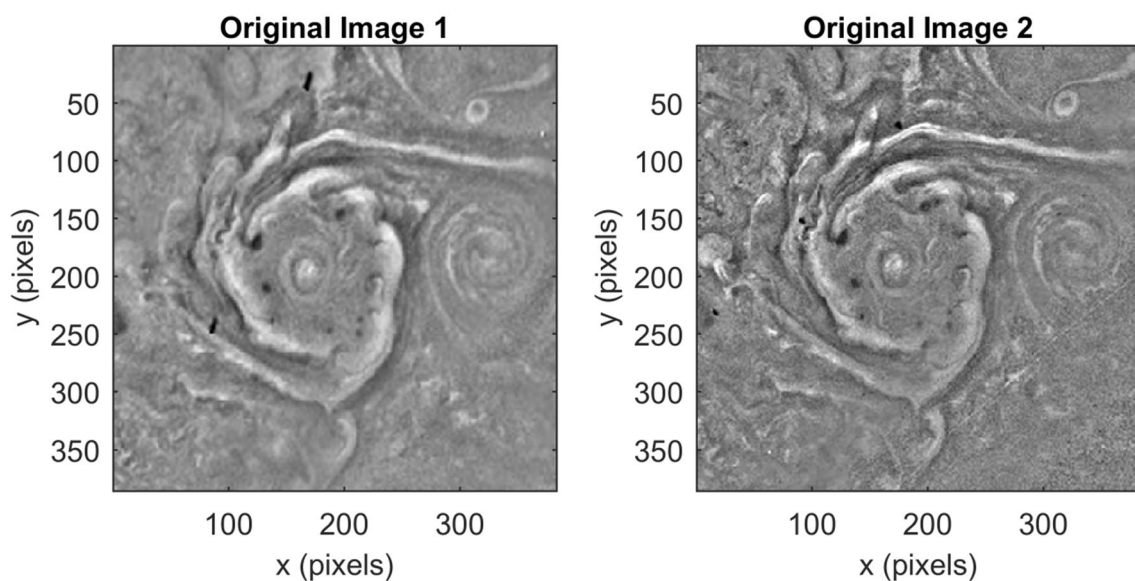

Fig. 5 A pair of the original cloud images of a cyclone acquired by JunoCam

(such as 1–10 h). As a result, a vortex in a planetary atmosphere could move significantly in the image plane even after image navigation is applied to images to align the region of interest on the planetary surface. For example, Fig. 5 shows a pair of cloud images of a circumpolar cyclone in the north-pole (NP) region of Jupiter acquired by the JunoCam (Hansen et al. 2017). The data for this view of one of Jupiter's circumpolar cyclones in the NP region from JunoCam's 28th orbit are extracted from JNCR_2020207_28C00008_V01 and JNCR_2020207_28C00010_V01 in the website of Planetary Virtual Observatory & Laboratory (http://pvol2.ehu.eus/junocam/PJ28/). The data were processed by Shawn Brueshaber (private communication) using the software ISIS3 (https://isis.astrogeology.usgs.gov/). These have been map-projected (polar stereographic) to a pixel resolution of 20 km/pixel. The time interval between them is 360.3 s. There is a significant shift between the original image 1 and image 2. To extract the rotation motion of the flow, the shift should be corrected by image registration before cloud tracking.

An iterative optical-flow-based image registration scheme is proposed to correct the non-flow-related motion between images acquired by a moving camera before flow estimation. First, OFM is applied to the original image pair, and the domain-averaged displacement is calculated in a region of interest around the center of the vortex to provide an initial value of the image shift of the vortex center. Then, by using an image shifting scheme, the original image 1 is translated based on the initially estimated shift to produce a shifted image 1. The image shifting scheme uses an evolution equation for subpixel movement in addition to applying a translation transformation. Then,

a Gaussian filter is applied to remove some noise caused by the shifting process. Further, OFM is applied to a pair of the shifted image 1 and the original image 2 to calculate a second image shift and generate a second shifted image 1. This process is iterated until the estimated displacement is smaller than a pre-set threshold value. This scheme will generate the rotational motion of the flow and the displacement of the vortex center. Figure 6 shows the shifted image 1 after 8 iterations and the original image 2, where both the images are filtered by using a Gaussian filter with a
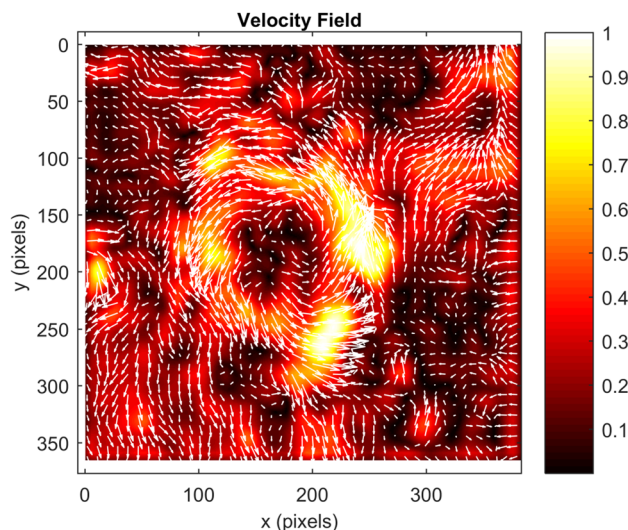

Fig. 7 The velocity field extracted from a pair of the cloud images of a cyclone after 8 iterations, where the velocity magnitude is normalized by its maximum value
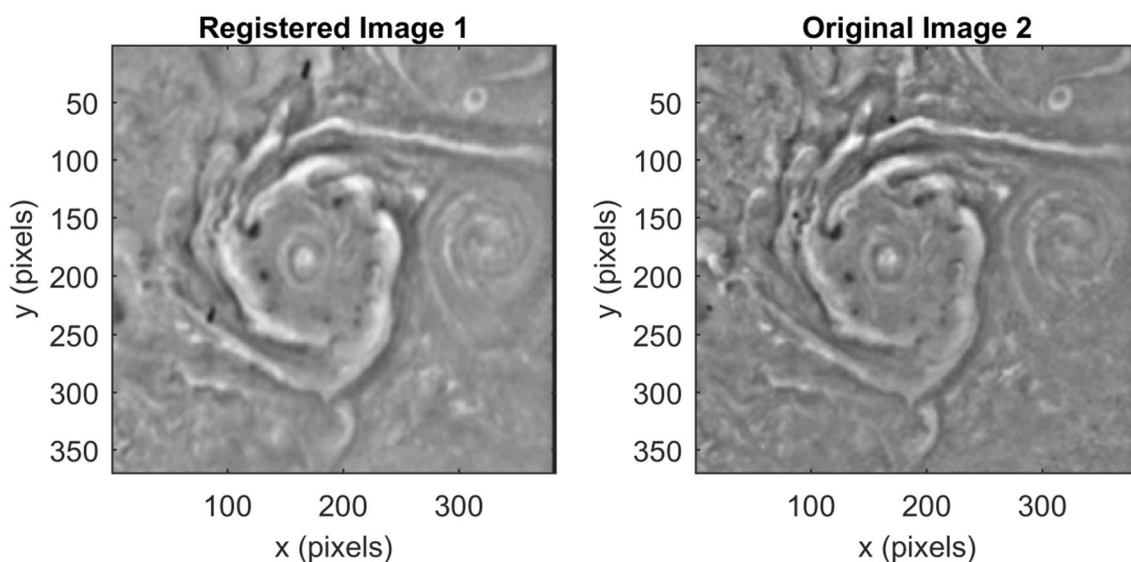

Fig. 6 The shifted image 1 after 8 iterations and the original image 2 of a cyclone acquired by JunoCam

standard deviation of 4 pixels. The resulting velocity field after 8 iterations is shown in Fig. 7.

2.3 Metric conversion from image to surface

Conversion of the image coordinates to the ellipsoidal surface coordinates is described below. In some literature of the planetary sciences, the planetocentric latitude ϕ_c is used for mapping, which is the angle between the connecting line between the center of a planet and a point on the planet surface and the equatorial plane. The planetocentric latitude ϕ_c is related to the planetographic latitude by $\phi_g = \tan^{-1}\left[(a/b)^2 \tan\phi_c\right]$, where a and b are the equatorial and polar radii of the planet, respectively. The distance between a point of the surface and the rotational axis of the planet is denoted by $r(\phi_g)$, and the radius of the curvature of the local meridian is denoted by $R(\phi_g)$. The mapping factors in the ellipsoidal surface coordinates are given by

$$r(\phi_g) = \frac{a}{\left(1 + (b/a)^2 \tan^2\phi_g\right)^{1/2}}, \quad R(\phi_g) = \frac{r(\phi_g)/\cos\phi_g}{\sin^2\phi_g + (a/b)^2 \cos^2\phi_g}. \tag{6}$$

In general, for metric conversion, the differential displacements along the coordinate curves on the surface are given by

$$dx = r(\phi_g)d\lambda, \quad dy = R(\phi_g)d\phi_g. \tag{7}$$

As an example, we consider the polar-projected images of Saturn's north pole vortex (NPV), which were captured by the Narrow-Angle Camera on board the Cassini spacecraft over a period of 5 h and 19 min. on November 27, 2012 (Sayanagi et al. 2017; Liu et al. 2019). The top visible cloud layer that is about 100 km below the top of the troposphere is made of ammonia clouds. The interval between consecutive images varies from 20.5 to 29.1 min. Figure 8 shows the first pair of the 14 NPV images. In this special case where the origin of the surface coordinate system (x, y) is located at the north pole (NP), a relevant relation is $dx = dy = R(\phi_g)d\phi_g$. For Saturn, $a = 60,268$ km and $b = 54,364$ km (Seidelmann et al. 2002). For the images, a projection scaling factor is $\Delta\phi_g = 0.002844\pi/180$ rad/pixel. According to Eq. (6), a converting factor in the image plane in both the x and y coordinates is about 3316 m/pixel near the NP ($\phi_c = 80°–90°$) since the core of the NPV is at the apex of the ellipsoid (Saturn) and the center of the image plane.

Figure 9 shows the time-averaged velocity vectors and relative vorticity field of the NPV, which illustrates the overall flow structure in the cyclonic inner core of Saturn's NPV. The result in Fig. 9 is obtained by averaging 13 instantaneous velocity fields obtained from the sequence of 14 images. Figure 10 shows the profiles of the zonal velocity and the meridional velocity as functions of the planetocentric latitude, where the result is obtained by further averaging the velocity data azimuthally over 360°. The profile of the zonal velocity is consistent with that extracted by using CIV with interrogation windows of 30×30 pixels (about 60 km $\times$ 60 km in the physical space) for computation of cross-correlation (Sayanagi et al. 2017). The peak velocity of 150 m/s given by CIV is about 17% slower than that calculated in the current work using the optical flow method. The location of the peak zonal wind is at $\phi_c = 88.95°$ N latitude, which
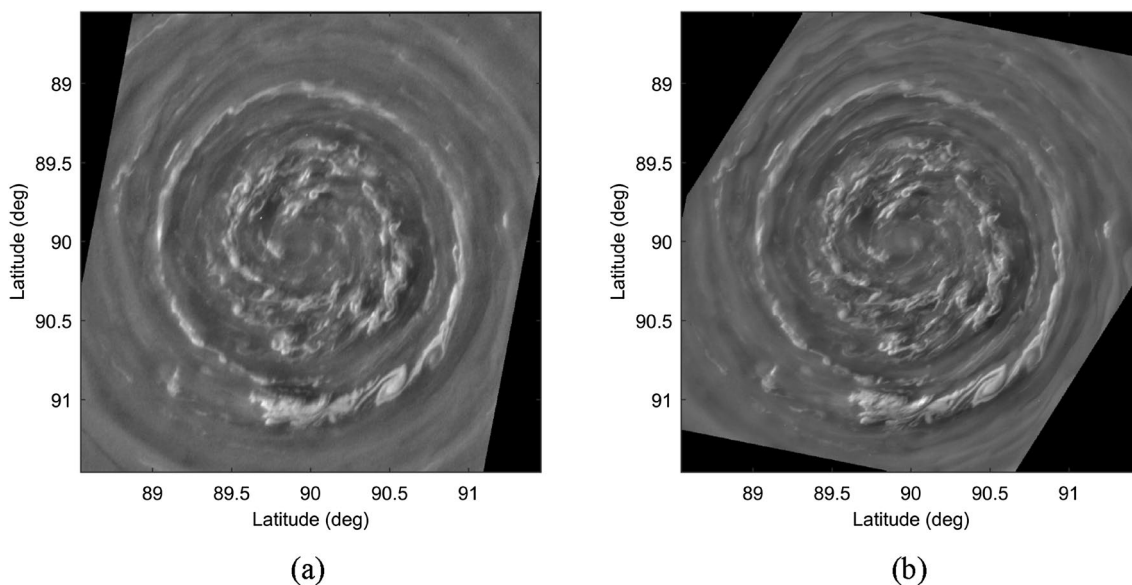

(a)

(b)

Fig. 8 The first pair of cloud images of Saturn's north-pole vortex (NPV), where the time intervals between them is 21.9 min. From Liu et al. (2019)
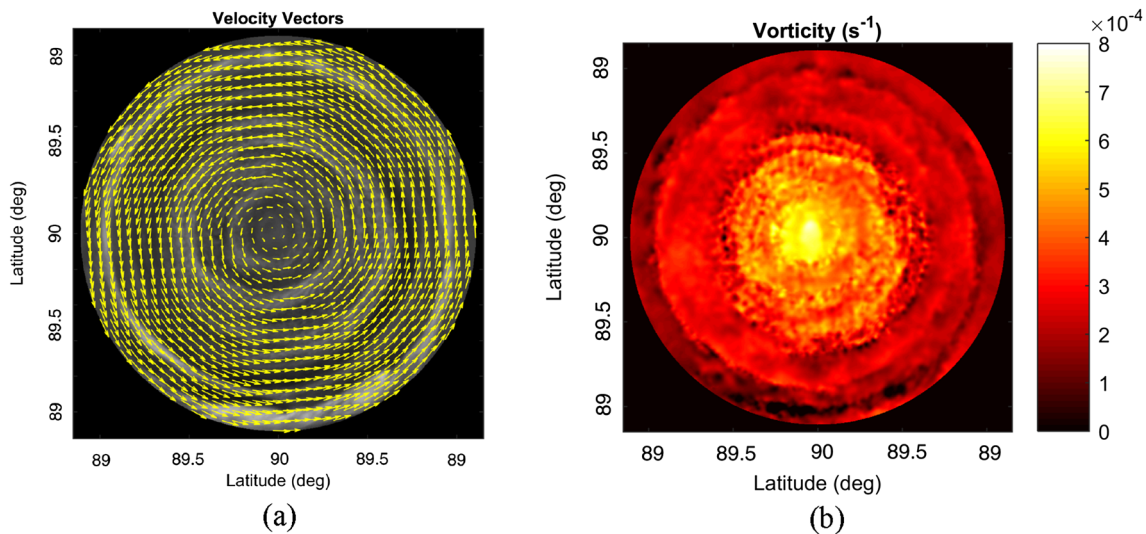
Fig. 9 The time-averaged flow field of Saturn's NPV: **a** velocity vectors, and **b** relative vorticity. From Liu et al. (2019)
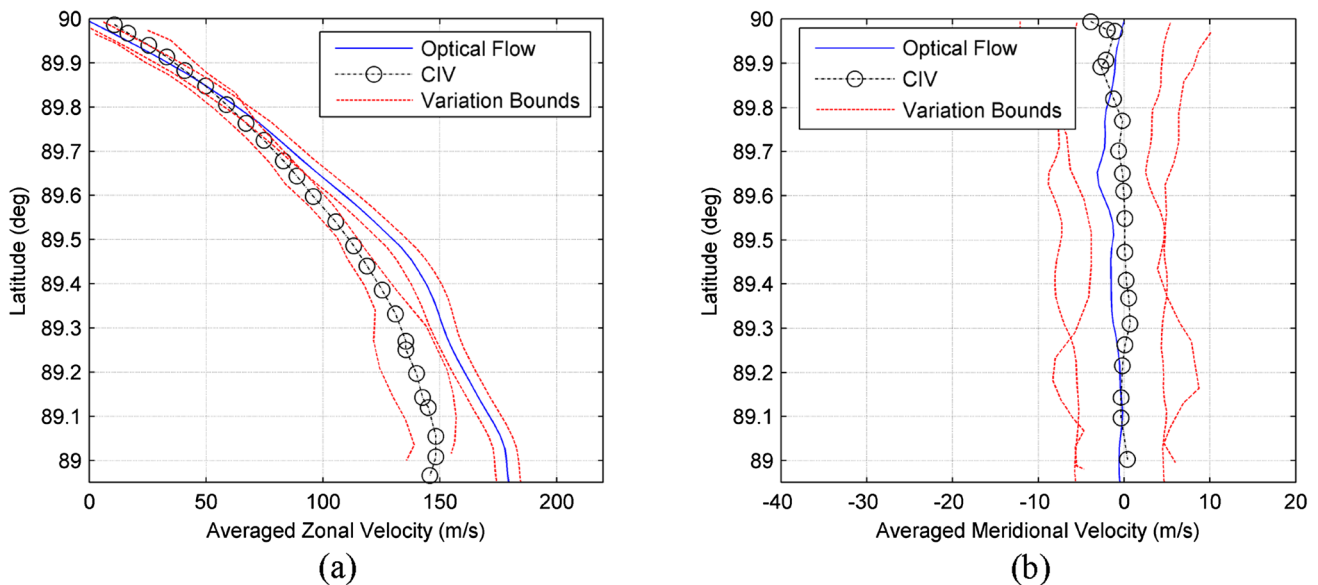

Fig. 10 The mean profiles of the NPV: **a** the zonal (circumferential) velocity and **b** the meridional velocity. From Liu et al. (2019)

is consistent with the value given by Sayanagi et al. (2017) and Antuñano et al. (2015, 2018). The variation bounds indicated in Fig. 10 mainly represent the temporal-spatial changes of the velocity structures in ensemble averaging and averaging over a polar angle range.

3 Manual cloud tracking

Manual tracking is a simple intuitive method conducted by visually inspecting a sequence of cloud maps. In manual cloud tracking, cloud displacement vectors are extracted

from image pairs by visually identifying distinct cloud features, typically yielding 100–1000 vectors depending on the richness of features. Wind velocity vectors are obtained by dividing the displacement of a cloud feature with a time interval, assuming that the feature is a passive scalar transported by the flow. Manual tracking can be used to track planetary cloud features over time separations as large as 10 h (one rotation time of Jupiter). The human eyes can usually follow the cloud motion over a 10-h period and choose corresponding tie-points by eyes reasonably well. However, manual tracking has some shortcomings. Hand-derived velocity fields are irregularly distributed on

sparse locations. Sub-pixel accuracy in determining displacement vectors cannot be obtained. Identification of a pair of corresponding cloud features in two sequential images is somewhat subjective, which could lead to wrong point correspondence.

Manual cloud tracking has been used to obtain valuable velocity fields of the GRS, WOs and other large planetary vortices (Mitchell et al. 1981; Dowling and Ingersoll 1988; Sada et al. 1996; Vasavada et al. 1998; Simon-Miller et al. 2002; Legarreta and Sánchez-Lavega 2005). Using manual cloud tracking, Mitchell et al. (1981) determined the velocity fields within the GRS and WO BC from sequences of Voyager 1 images. Dowling and Ingersoll (1988) further

processed the Voyager images to obtain velocity vectors of the GRS. Figure 11a shows a Voyager 2 image of the GRS, where the planetographic latitude and longitude are labeled. Figure 11b shows velocity vectors (more than 2000) at irregular locations obtained from Voyager 1 and 2 images using manual cloud tracking. From Fig. 11b, the unique structure of the GRS has a high-speed anti-cyclonic elliptical collar and a relatively quiescent inner region. In this sense, the GRS is considered as a "hollow" vortex. The velocity data were interpolated on a regular grid, and then the potential vorticity and divergence fields were calculated.

From the Voyager 1 and 2 images of the GRS, Sada et al. (1996) obtained velocity fields (about 1200 vectors),

Fig. 11 Typical GRS image and velocity vectors obtained by manual cloud tracking: **a** Voyager 2 image taken on July 5, 1975, and **b** velocity vectors (more than 2000). From Dowling and Ingersoll (1988)

(a)

(b)
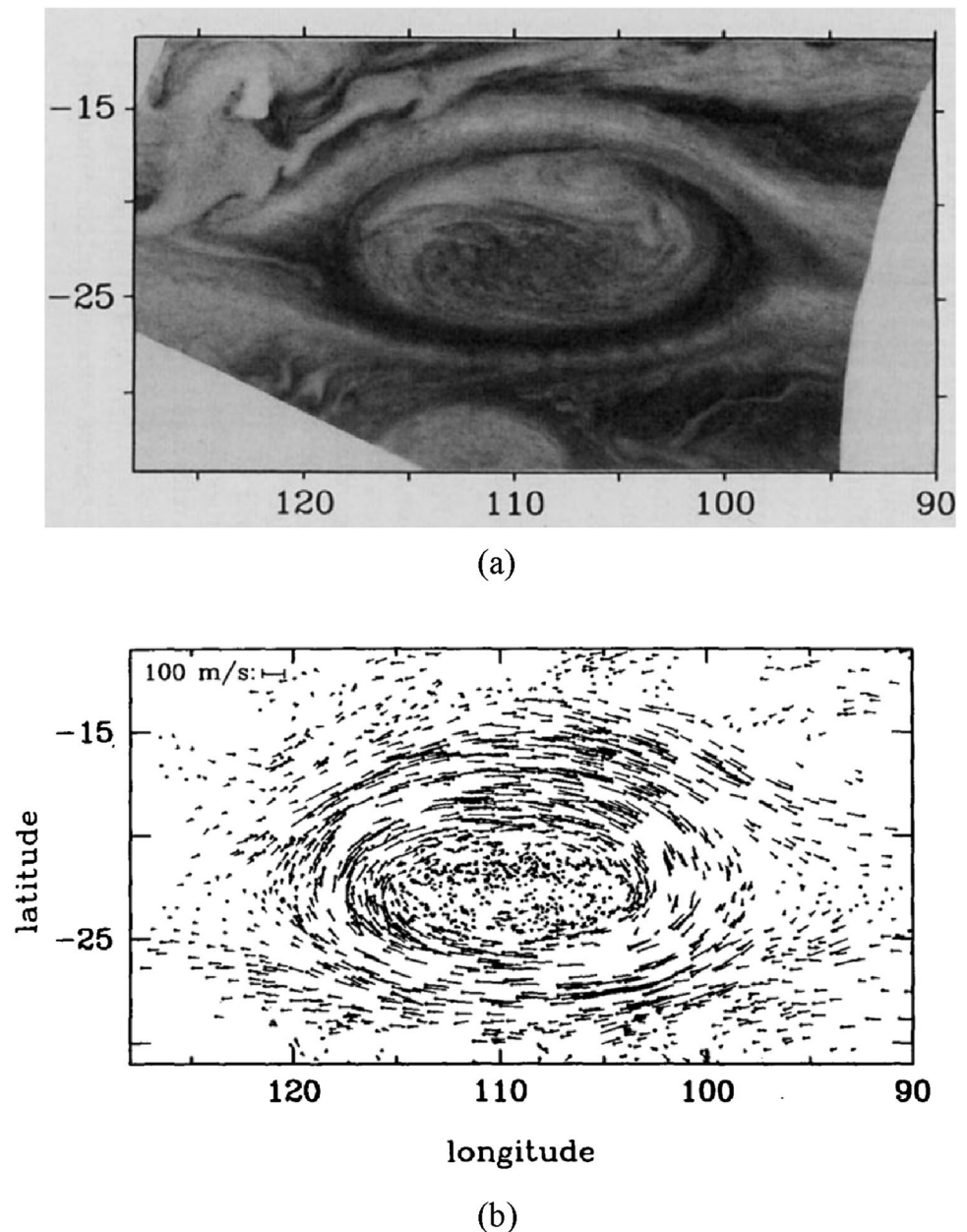
focusing on the low-speed inner region of the GRS. It was observed that there was a coherent motion in apparently 2D turbulent flow near the central region where upwelling and outflow of material were present. The velocity profiles across the GRS are shown in Fig. 12, which were obtained by Sada et al. (1996) using manual cloud tracking. Figure 12a shows the east–west components of all velocity vectors within 1° of the north–south axis (109.5° longitude) of the GRS, indicating a twisted structure of the velocity profile at the center. Based on this observation, Sada et al. (1996) inferred that there was a coherent cyclonic motion of fluid near the center of the GRS in the pseudo-random background. Figure 12b shows the north–south components of all velocity vectors within 1° of the east–west axis (23° S planetographic latitude) of the GRS. In contrast to Fig. 12a, Fig. 12b does not show the cyclonic motion at the center. This means that the motion near the center is more complex. Due to the low resolution of this hand-derived velocity data, it is difficult to accurately identify dynamical characteristics such as the behavior of the flow near the center and the magnitudes and locations of the velocity peaks along the axes.

4 Correlation image velocimetry

Correlation image velocimetry (CIV) is an automated method in which a computer algorithm finds matching features by correlating small windows of pixels in two cloud images (Rossow et al. 1990; Toigo et al. 1994; Tokumaru and Dimotakis 1995; Fincham and Spedding 1997; Read et al. 2005, 2006; Choi et al. 2007; Wong et al. 2021). In a certain sense, CIV is an adapted version of PIV for continuous pattern images. Similar to PIV, where the flux of particles across a laser illumination domain is considered

as a small error, it is assumed that CIV is robust enough to account for the creation and dissipation of planetary clouds. In CIV, spatial cross-correlation is calculated between continuous patterns in windows rather than discrete particles. Thus, the values of correlation are usually lower than those in PIV, which could generate many spurious velocity vectors for images lacking distinctly trackable features. Spurious velocity vectors are removed manually or automatically in CIV.

Choi et al. (2007) applied a two-pass CIV (with a 100-pixel correlation window in the first pass and a 10-pixel correlation window for the second pass) to three observations of the GRS at approximately 1-h intervals taken during the 28th orbit of Galileo (G28) using the Solid State Imaging (SSI) Camera. Figure 13a shows one of three May 2000 Galileo mosaics. From the Galileo mosaics with 1-h and 2-h separations, they produced a GRS velocity field made up of about 30,000 vectors, as shown in Fig. 13b. CIV is able to resolve the GRS high-speed collar, the relatively calm central region, and jets to the south and northwest of the GRS. Figure 14 shows the zonal and meridional velocity profiles of the GRS in its axes. The zonal velocity profile was averaged by taking measurements within 1.5° longitude of the central meridian of the GRS in the G28 dataset (− 5.8° W) and average over 0.25° bins in latitude. The meridional velocity profile was generated in a similar manner by taking measurements within 1.5° latitude of 20° south planetocentric latitude and averaging over 0.25° bins in longitude. The maximum tangential velocity given by Choi et al. is about 170 m/s along the southern edge of the GRS. Overall, the velocity profiles given by Choi et al. from the G28 data are similar to the profiles calculated by Vasavada et al. (1998) from the data obtained during the 1st orbit of Galileo (G1), Dowling
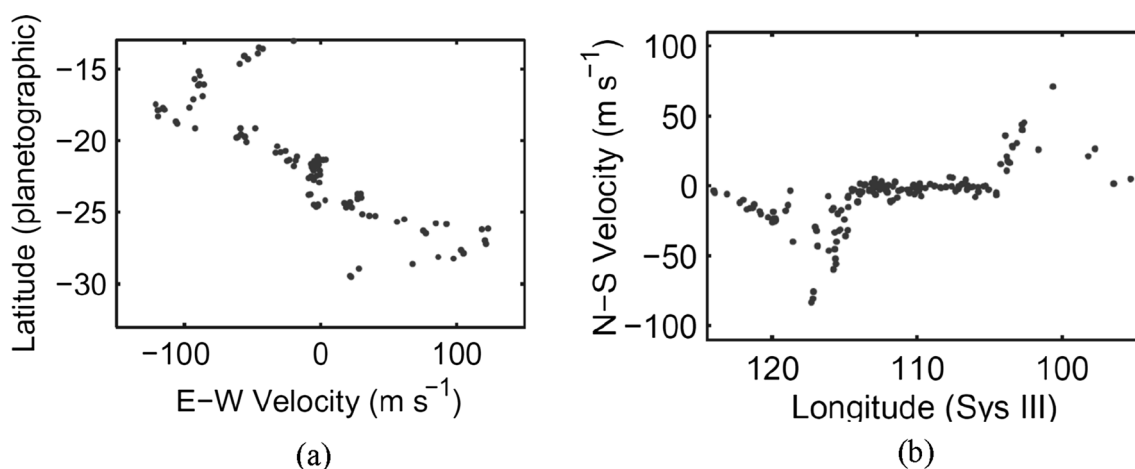

(a)

(b)

Fig. 12 Velocity profiles across the GRS obtained by Sada et al. (1996) using manual cloud tracking: **a** the east–west components of all velocity vectors within 1° of the north–south axis (109.5° longi-

tude) of the GRS, and **b** the north–south components of all velocity vectors within 1° of the east–west axis (23° S planetographic latitude) of the GRS. From Asay-Davis et al. (2009)
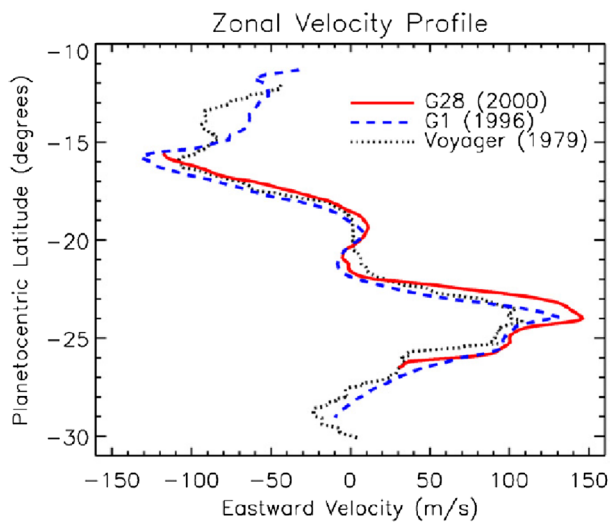
Fig. 13 GRS image and velocity vectors obtained by CIV: **a** one of three May 2000 Galileo mosaics, where the shadow in the mosaic belongs to Europa, and **b** wind velocity vectors of the GRS. Only a ninth of the total number of velocity vectors are shown in this figure for the sake of clarity. Note the scale vector at top right. From Choi et al. (2007)
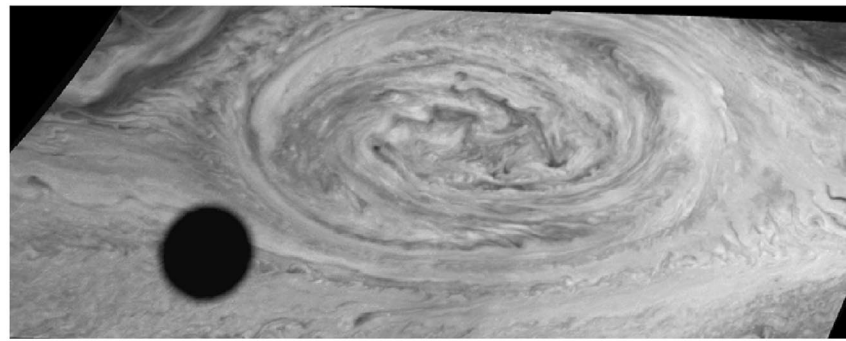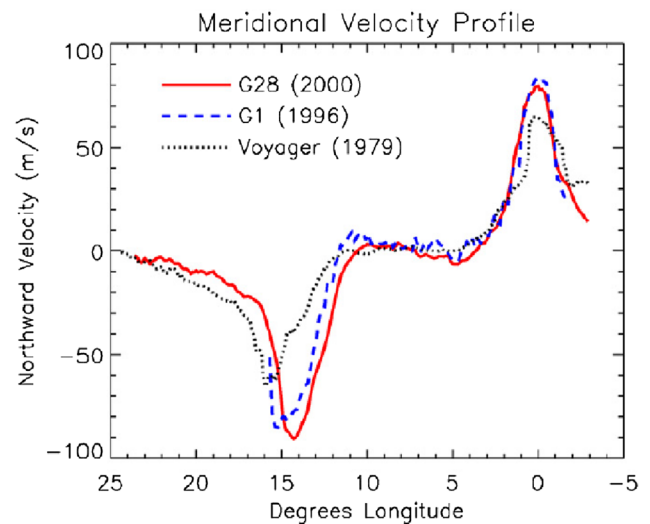

(a)
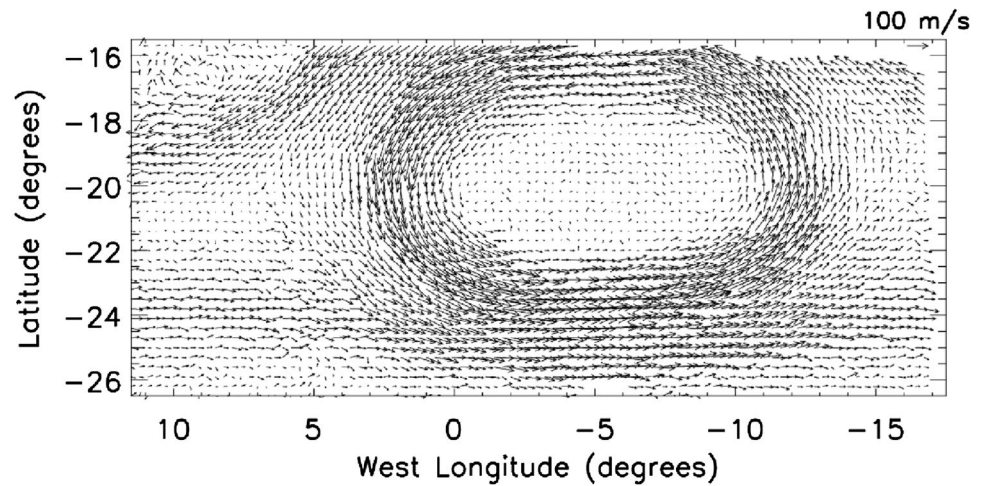
(b)

(a)

(b)

Fig. 14 Velocity profiles of the GRS in its axes obtained by CIV: **a** zonal (east–west) velocity, and **b** meridional (north–south) velocity. The solid line is calculated by Choi et al. (2007) from the G28 data. The velocity profiles from Vasavada et al. (1998) from the G1 data are shown as a dashed line. The dotted line is the Voyager data from Dowling and Ingersoll (1988). From Choi et al. (2007)

and Ingersoll (1988) from Voyager data, and Vasavada and Showman (2005) from Cassini data. The cyclonic rotation motion near the center of the GRS is revealed in Fig. 14a. These comparisons indicate that the basic structure of the GRS is persistent over a period of observations.

Asay-Davis et al. (2009) developed the Advection Corrected Correlation Imaging Velocimetry (ACCIV). In ACCIV, the CIV algorithm developed by Fincham and Spedding (1997) and Fincham and Delerce (2000) is used as a subroutine, where to decrease systematic errors, a second pass is applied to track features to a precision smaller

Fig. 15 Velocity vectors derived by ACCIV from the HST_GRS_06 dataset using images separated by about 10 h. For clarity, 3000 out of the 140,000 velocity vectors are displayed. From Asay-Davis et al. (2009)

than a pixel. The velocity obtained from the first pass is used to generate a deformed window in the second image according to a linear transformation intended to take into account small deformations by the flow. Several steps are implemented in ACCIV. First, an initial set of velocity vectors is generated by either applying CIV or manual tracking. Then, based on the initial velocity field, cloud features are numerically advected by moving the pixels in the first (or second image) forward (or backward) to a mid-point in time. The next step is tracking each feature forward or backward in time to find its location in the original images. The key step determines the path of a cloud feature between the first and second images using a linear interpolation and producing a new velocity field by tracing the path iteratively. ACCIV was applied to the HST image pair of the GRS, yielding about 140,000 velocity vectors as shown in Fig. 15. Figure 16 shows the velocity profiles of the GRS from ACCIV applied to the HST_GRS_06 dataset. Figure 16a shows the east–west components of all velocity vectors within 0.2° of the north–south axis of the GRS, and Fig. 16b shows the north–south components of all velocity vectors within 0.2° of the east–west axis (23° S planetographic latitude) of the GRS. The data obtained by ACCIV were used to study the interaction of GRS and zonal jet streams (Shetty et al. 2007).

CIV has been used to study the atmospheric flow structures near Saturn's north and south poles (NP and SP) (Lindal et al. 1985; Godfrey 1988; Sánchez-Lavega et al. 2006; Baines et al. 2007, 2009; Fletcher et al. 2008; Dyudina et al. 2009; Sayanagi et al. 2019; Studwell et al. 2018). In particular, recent studies have focused on the stable cyclonic vortex centered at the north pole (NPV), extending from 85° N to the north pole with zonal winds of order of about
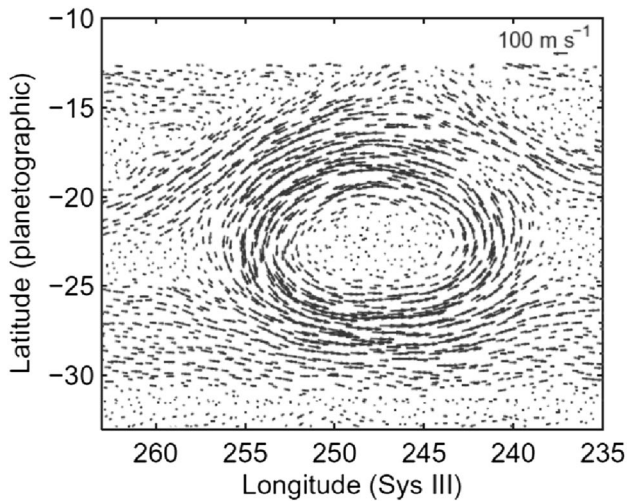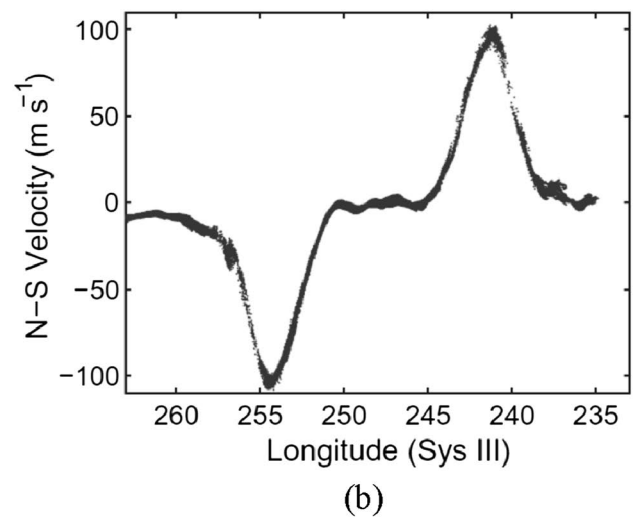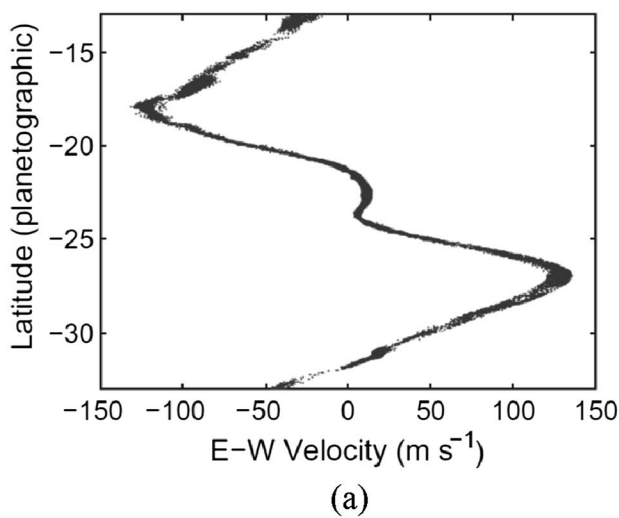

(a)

(b)

Fig. 16 Velocity profiles of the Great Red Spot in tits axes from ACCIV applied to the HST_GRS_06 dataset: **a** the east–west components of all velocity vectors within 0.2° of the north–south axis

(248° longitude) of the GRS, and **b** the north–south components of all velocity vectors within 0.2° of the east–west axis (23° S planetographic latitude) of the GRS. From Asay-Davis et al. (2009)

100 m/s (Antuñano et al. 2015, 2018; Sayanagi et al. 2017). The zonal and meridional wind profiles as well as vorticity and divergence fields of the NPV were measured using CIV from images of Saturn obtained during different orbits of the Cassini spacecraft. However, prior studies using CIV had many void regions in their velocity measurements where no trackable features were detected (Sayanagi et al. 2017).

5 Optical flow method

The optical flow method (OFM) is suitable for planetary cloud tracking since the optical flow equation is derived from the fundamental equations of fluid mechanics (Liu et al. 2012a, b, 2019). We consider the light scattering process through flow containing light-scattering particles in a cloud layer confined by the lower and upper control planes Γ_1 and Γ_2 that are located at the top and bottom of the cloud layer, respectively. For the motion of cloud particles (or aerosols), the disperse phase number equation is $\partial N_p / \partial t + \nabla \cdot (N_p \boldsymbol{U}) = 0$, where $\boldsymbol{U} = (U_1, U_2, U_3)$ is the particle velocity in a 3D object space and N_p is the number of particles per unit total volume. By projecting the disperse phase number equation onto the image plane, the optical flow equation in the image plane can be derived (Liu and Shen 2008). The optical flow equation is written as

$$\frac{\partial I_N}{\partial t} + \nabla \cdot (I_N \boldsymbol{u}) = F(x_1, x_2), \tag{8}$$

where I_N is the normalized image intensity, $\boldsymbol{u}$ is the optical flow, $\nabla = \partial / \partial x_i \ (i = 1, 2)$ is a gradient operator in the image plane, and the boundary term $F = w_{\text{ext}} \langle C_{\text{ext}} \rangle_a \boldsymbol{n} \cdot (N_p \boldsymbol{U}) \big|_{\Gamma_1}^{\Gamma_2}$ acts as a source/sink term representing the effect of particles accumulated within a cloud layer confined by Γ_1 and Γ_2. The optical flow in Eq. (8) is defined as $\boldsymbol{u} = (u_1, u_2) = \gamma \langle \boldsymbol{U}_{12} \rangle_N$, where $\langle \boldsymbol{U}_{12} \rangle_N$ is the light-path-averaged particle velocity defined as

$$\langle \boldsymbol{U}_{12} \rangle_N = \int_{\Gamma_1}^{\Gamma_2} N_p \boldsymbol{U}_{12} \, dX_3 \Big/ \int_{\Gamma_1}^{\Gamma_2} N_p \, dX_3, \tag{9}$$

$\boldsymbol{U}_{12} = (U_1, U_2)$ is the velocity vector parallel to the image plane, and γ is a constant scaling factor in the orthographical projection transformation from the 3D object space onto the image plane. Physically, the optical flow represents the light-path-averaged velocity of particles in a cloud layer. It is noted that Héas et al. (2007) derived an optical flow equation similar to Eq. (8) from the continuity equation with a variable density for layered estimation of atmospheric mesoscale dynamics from satellite imagery.

The lower and upper control planes Γ_1 and Γ_2 are idealized surfaces for certain physical boundaries. For images of

planetary clouds that scatter and reflect the sunlight, the upper control plane Γ_2 is placed at the top of clouds. The lower control plane Γ_1 is placed at the interior location with the depth of penetration of the sunlight through clouds, depending on the light absorption and scattering of cloud particles. In most cases, the thickness between Γ_1 and Γ_2 is much smaller than the length scale of the imaged surface region. In a thin layer of clouds, the inflow and outflow of mass through Γ_1 and Γ_2 tend to be balanced (their sum is small) due to the mass conservation. Furthermore, for most planetary flows such as in jet streams and planetary vortices, the velocity parallel to the surface is much larger than the vertical velocity component. Therefore, $\boldsymbol{n} \cdot (N_p \boldsymbol{U}) \big|_{\Gamma_1}^{\Gamma_2}$ can be neglected compared to the convection term in Eq. (8). The above discussions provide a physical foundation of OFM applied to cloud tracking. Originally, OFM in computer vision tends to estimate apparent motions of objects in images regardless of their physical origins, and thus the physical meaning of the optical flow in a specific problem cannot be clearly elucidated.

For a pair of cloud images where I_N is a measurable quantity, an inverse problem is to determine the optical flow $\boldsymbol{u}$. To solve for the optical flow from Eq. (8), a variational formulation with a smoothness constraint is used (Horn and Schunck 1981; Liu and Shen 2008; Heitz et al. 2010; Wang et al. 2015; Liu et al. 2015). Given I_N and F, we define a functional

$$J(\boldsymbol{u}) = \left\| \frac{\partial I_N}{\partial t} + \nabla \cdot (I_N \boldsymbol{u}) - F \right\|_2 + \alpha (\|\nabla u_1\|_2 + \|\nabla u_2\|_2), \tag{10}$$

where $\| \|_2$ denotes the L^2-norm on an image domain D, the first term is an equation functional, the second term is a first-order Tikhonov regularization functional, and α is a Lagrange multiplier.

Minimization of the functional $J(\boldsymbol{u})$ leads to the Euler–Lagrange equation

$$I_N \nabla \left[\frac{\partial I_N}{\partial t} + \nabla \cdot (I_N \boldsymbol{u}) - F \right] + \alpha \nabla^2 \boldsymbol{u} = 0, \tag{11}$$

where $\nabla^2 = \partial^2 / \partial x_i \partial x_i \ (i = 1, 2)$ is the Laplace operator. When a pair of temporally separated images is given and F is neglected in a first-order approximation, a standard finite difference method can be used to solve Eq. (11) with the Neumann condition $\partial \boldsymbol{u} / \partial n = 0$ on the image domain boundary ∂D for the optical flow.

A standard finite difference method is used to solve Eq. (11) (Wang et al. 2015). The optical flow algorithm applies the Horn–Schunck estimator for an initial solution (Horn and Schunck 1981) and applies the Liu-Shen estimator for a refined solution (Liu 2017). There is no rigorous method to determine the Lagrange multiplier a priori (Cai

et al. [2018](#)). For a specific flow, trial-and-error tests can be conducted through simulations to determine an optimal value of the Lagrange multiplier. In a certain range of the Lagrange multiplier, optical flow solution is not very sensitive to the Lagrange multiplier. Other relevant parameters are the number of iterations in successive improvement of the optical flow solution, and the sizes of the Gaussian filters to compensate for the artifacts introduced by illumination variation and noise in pre-processing. In an ideal case where illumination is time-independent, no Gaussian filter is applied. Liu et al. ([2015](#)) discussed how to tune the Gaussian filter sizes. For extraction of large displacements in the image plane, a coarse-to-fine scheme is applied to reduce the error in optical flow computation (Liu [2017](#)). Using OFM, Liu et al. ([2012a](#), [b](#), [2019](#)) obtained high-resolution velocity fields of Jupiter's GRS and Saturn's NPV. Effort has been made to apply different versions of OFM to satellite images of geophysical flows on Earth (Auroux and Fehrenbach [2011](#); Ravela et al. [2010](#); Cui et al. [2013](#); Wu et al. [2016](#); Héas et al. [2007](#), [2012](#), Héas and Mémin [2008](#)).

An open source optical flow program in Matlab, "OpenOpticalFlow," is described by Liu ([2017](#)) for extraction of high-resolution velocity fields from various flow visualization images (https://github.com/Tianshu-Liu/OpenOpticalFlow). In addition, an open source Matlab program, "OpenOpticalFlow_PIV," integrates OFM with the cross-correlation method for extraction of high-resolution velocity fields from particle images with large displacements (Liu and Salazar [2021](#)) (https://github.com/Tianshu-Liu/OpenOpticalFlow_PIV_v1). This hybrid method provides an additional tool to process cloud images with many distinct features, which combines the advantages of OFM and cross-correlation method and overcomes the intrinsic issues of the two methods.

6 Comparisons between different cloud-tracking methods

To evaluate the accuracy of cloud tracking, multiple cloud-tracking methods are examined based on synthetic wind data, and the velocity fields measured using these methods compare against the "truth" to evaluate their accuracy. A synthetic velocity field is reconstructed by superposing the elemental flow structures to simulate the flow field of the GRS (Liu et al. [2012a](#), [b](#)). The first structure is a 2D elliptical closed-loop jet that is generated to simulate the high-speed collar. The cross-sectional velocity distribution of the jet along the dividing ellipse is given by the Bickley jet distribution $U(n)/U_{\max} = \mathrm{sech}^2\left(n/L_0\right)$, where n are the transverse coordinate normal to the dividing ellipse. The ratio between the major axis (a) and minor axis (b) of the dividing ellipse is $a/b = 1.75$ and the half-width of the Bickley jet is

$L_0 = 0.285\,a$. The values of the major axis a and the maximum velocity $U_{\max}$ can be suitably chosen in simulations depending on the size of the GRS image and the maximum displacement in pixels. For a GRS image of 900×1200 pixels, $a = 436$ pixels and $U_{\max} = 15$ pixels/unit-time are used in simulations. To simulate the cyclonic rotation near the center of the GRS, a clockwise-rotating Oseen vortex is superposed at the center of the GRS, where the circumferential velocity is given by $u_\theta = (\Gamma/2\pi\,r)\left[1 - \exp\left(-r^2/r_0^2\right)\right]$, and the vortex strength is $\Gamma = -1000$ pixel^2/unit-time and the vortex core radius is $r_0 = 50$ pixels. Further, to simulate the complex small-scale structures in the inner region, 14 counterclockwise-rotating Oseen vortices are randomly distributed mainly in the inner region, where $\Gamma = 80$–700 pixel^2/unit-time and $r_0 = 10 - 20$ pixels. Two additional clockwise-rotating Oseen vortices are added in the collar. A typical synthetic velocity field is generated by superposition of all these flow structures, as shown in Fig. [17](#), where the maximum displacement is 16.4 pixels in the image plane.

A synthetic displaced image of the GRS (the synthetic image #2) is generated from the original the Galileo 1996 cloud images image #1 (900×1200 pixels) based on the synthetic velocity field using an image-shifting scheme that has a translation transformation and an evolution equation for subpixel motion. Since the synthetic flow field contains flow structures with a range of length scales, it can be used to examine the capability of different cloud-tracking methods to extract fine structures particularly in the inner region of the GRS.

From a pair of the synthetic GRS images, the velocity field is extracted using OFM (OpenOpticalFlow) (Liu [2017](#)), resulting in 900×1200 velocity vectors. Figure [18](#)a, b shows the velocity vector and normalized velocity magnitude fields extracted by OFM, respectively, where the fields are downsampled for clear illustration. In optical flow computation, the images are initially downsampled by 5 to obtain a coarse-grained velocity field, and then 4 iterations are carried out for successive improvement in both the accuracy and the spatial resolution. For comparison, a typical open-source Matlab PIV software, "PIVlab," is used to extract the velocity field (Thielicke and Stamhuis [2014](#)). The two-pass cross-correlation processing is used, where a 36-pixel and a 16-pixel windows are used in the first and second passes, respectively. Figure [19](#)a, b shows the velocity vector and normalized velocity magnitude fields extracted by PIVlab, respectively. Note that the extracted velocity field of 56×75 vectors is interpolated to form a field of 900×1200 vectors for comparison with the optical flow results. Further, a hybrid method is used, which includes a cross-correlation scheme (PIVlab) for initial estimation and an optical flow scheme for obtaining a refined high-resolution velocity field (Liu et al. [2020](#); Liu and Salazar [2021](#)). Figure [20](#)a, b shows
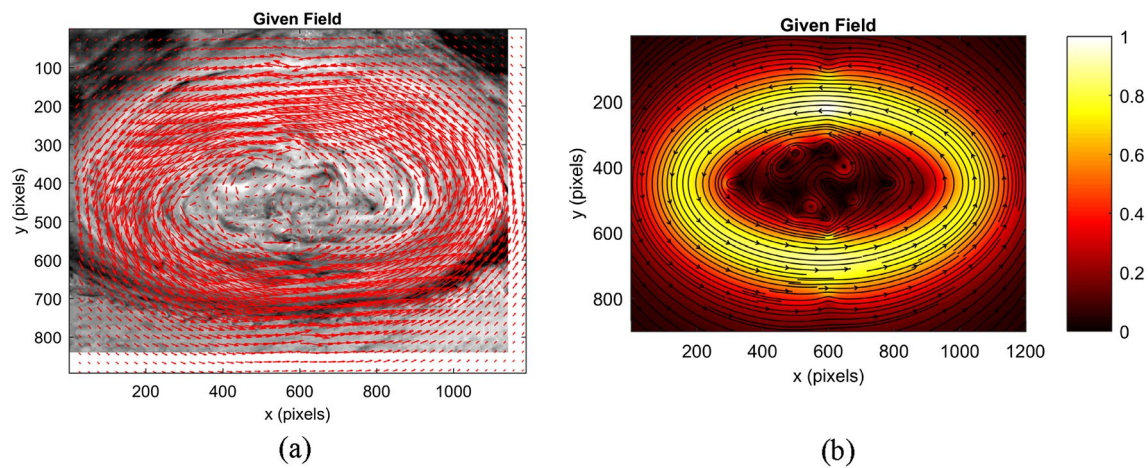
Fig. 17 The simulated velocity field of the synthetic GRS images: **a** velocity vectors superposed on a GRS image, and **b** velocity magnitude field with streamlines
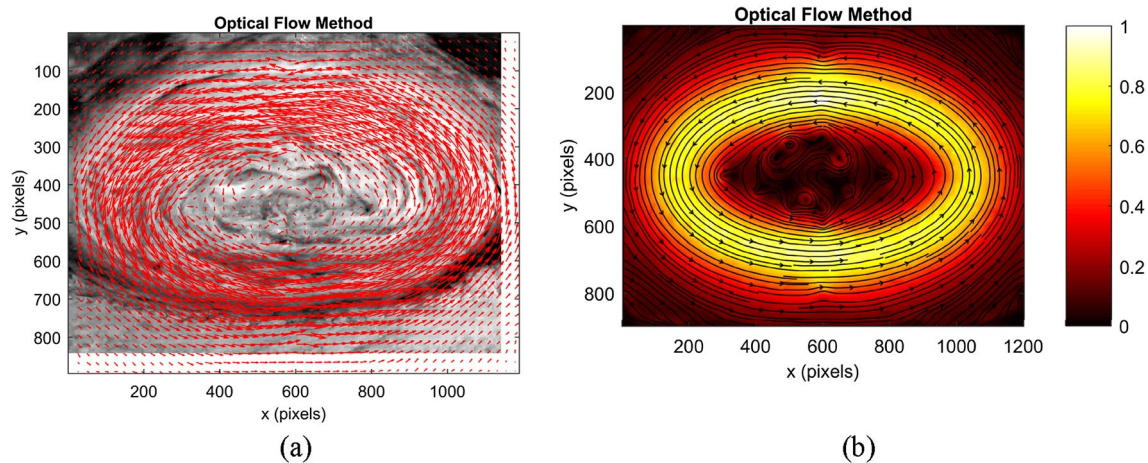

Fig. 18 The extracted velocity field of the synthetic GRS images by OFM: **a** velocity vectors superposed on a GRS image, and **b** normalized velocity magnitude field with streamlines

the velocity vector and normalized velocity magnitude fields extracted by the hybrid method, respectively.

Figure 21 shows comparisons between the velocity profiles across the center of the GRS in the *y*-axis (the minor axis) and *x*-axis (the major axis). These velocity profiles extracted by using OFM are in good agreement with the truth. In particular, the variations induced by the small-scale vortices are captured. The correlation method and hybrid method give similar results since the same correlation scheme is used as an essential element in these methods. Figure 22 shows the relative RMS velocity error in the whole image domain as a function of the maximum displacement for the different cloud-tracking methods, where the relative error is defined as the RMS error normalized the maximum displacement. The relative error is based on normalization

by the maximum velocity magnitude. OFM is more accurate than the other methods. Typically, the absolute RMS velocity error in the whole image domain for OFM is 0.34 pixels per unit time. The absolute RMS velocity error for the hybrid method is about 1.38 pixels per unit time in comparison with about 1.67 pixels per unit time for the correlation method. The accuracy of the hybrid method that was developed for improving PIV is limited by the accuracy of initial estimation using the correlation method. In general, the correlation method is not very suitable for images of continuous patterns like cloud images due to a lack of distinct trackable features.
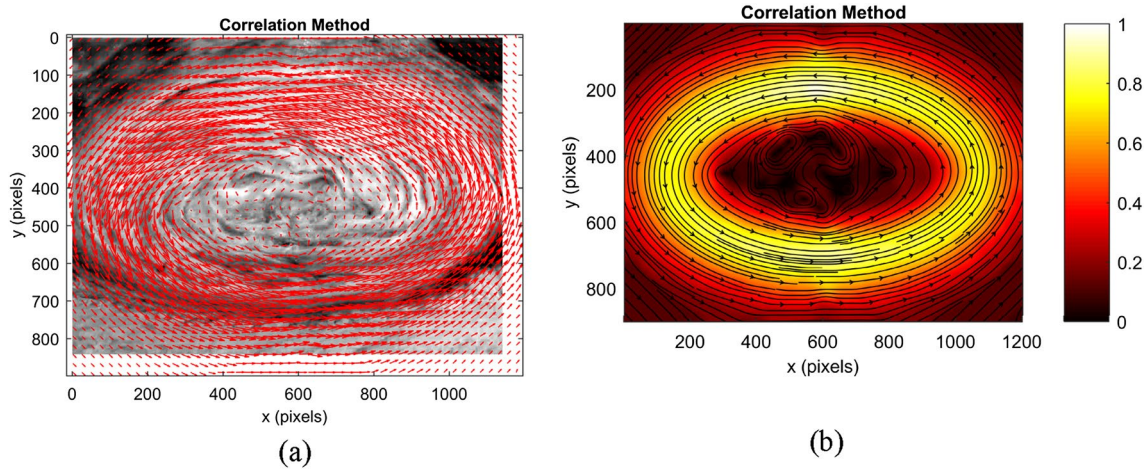
Fig. 19 The extracted velocity field of the synthetic GRS images by the correlation method: **a** velocity vectors superposed on a GRS image, and **b** normalized velocity magnitude field with streamlines
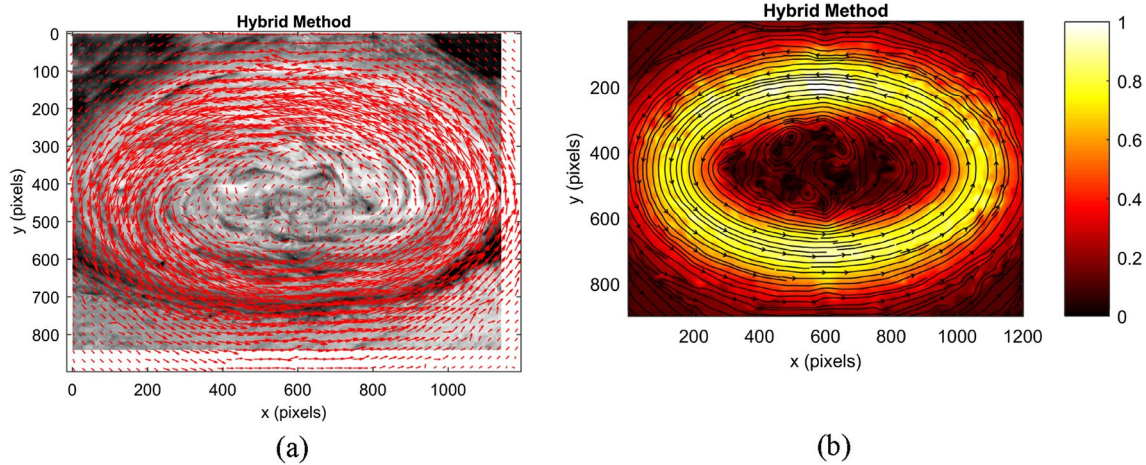

Fig. 20 The extracted velocity field of the synthetic GRS images by the hybrid method: **a** velocity vectors superposed on a GRS image, and **b** normalized velocity magnitude field with streamlines

7 Jupiter's great red spot

Using OFM, Liu et al. (2012a, b) obtained high-resolution velocity fields from the Galileo 1996 (the first orbit of Galileo denoted by G1) cloud images of the GRS and then studied the intrinsic flow structures of the GRS. Figure 23 shows the two images of the GRS with a time interval of 1.2 h (4320 s) between them. The size of the original images is 900×1200 pixels. Since the displacements in the images were rather large in the collar of the GRS, the original images were downsampled by 4 for optical flow computation that gives 231×302 velocity vectors. Figure 24a shows velocity vectors of the GRS, where the density of the vectors is reduced by 4 for the purpose of clear illustration. The

velocity vectors in the inner region are shown in Fig. 24b, exhibiting near-2D turbulence in the orthographically projected plane (parallel to the image plane).

The zonal velocity profile across the GRS during the G1 orbit is shown in Fig. 25a. The zero-zonal-velocity point is located at the latitude of about $-20.7°$, which corresponds to the node at the center of the GRS shown in Fig. 26c. For comparison, Fig. 25a also includes the data obtained by Vasavada et al. (1998) using both the manual tracking and correlation method and by Choi et al. (2007) using the correlation-based method. The zonal velocity profile given by OFM is consistent with those obtained by using other methods. The measured maximum tangential velocity is about 150 m/s in both the north and south sections of the collar at the latitudes of $-16°$ S and $-24°$ S, respectively.
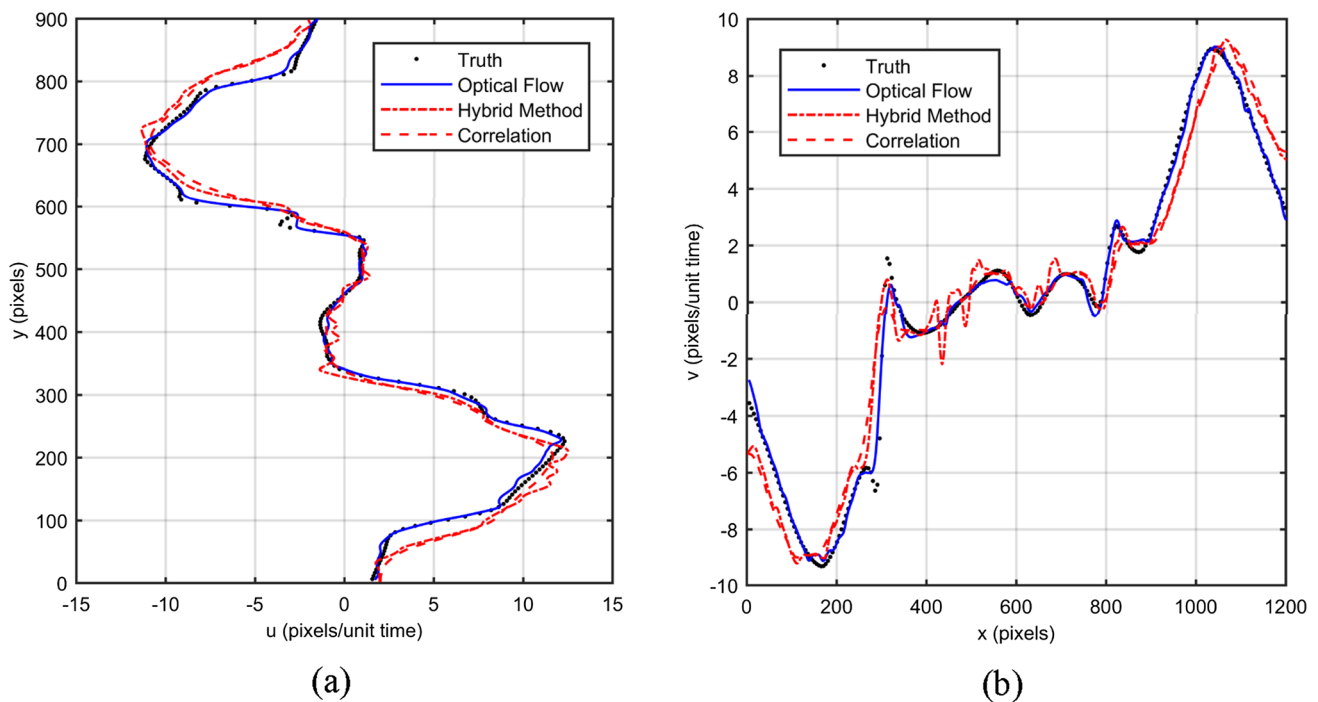
Fig. 21 The velocity profiles across the center of the synthetic GRS images: **a** *y*-axis (the minor axis), and **b** *x*-axis (the major axis)
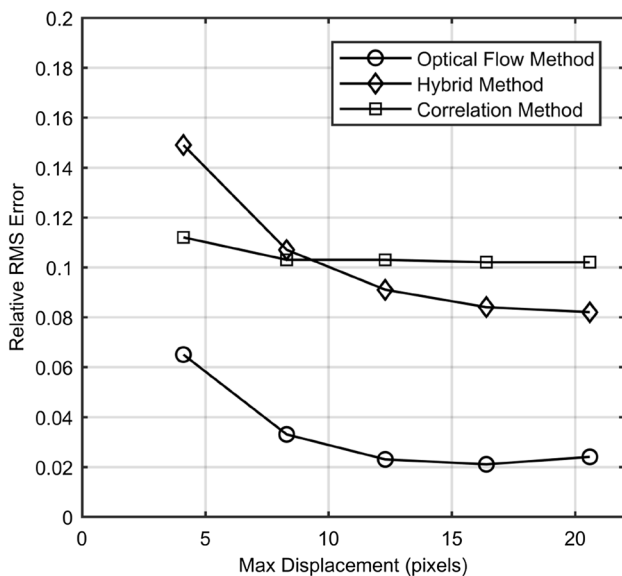

Fig. 22 The relative RMS error as a function of the maximum displacement for the different cloud-tracking methods

The optical flow estimation confirms the existence of the cyclonic rotation near the center of the GRS that was found in the previous measurements. Figure 25b shows the meridional velocity profiles across the GRS near the latitude of −20° S, where the data obtained by Choi et al. (2007) using the correlation method and by Asay-Davis et al. (2009) using

ACCIV are also included for comparison. The meridional velocity profiles do not indicate the corresponding cyclonic rotation. This implies that the cyclonic rotation shown in the zonal velocity profiles is associated with a non-axially symmetrical spiral flow structure rather than a simple vortex.

Figure 26a shows near-elliptical streamlines in the high-speed collar mainly confined in the two virtual elliptical boundaries. The inner and outer elliptical boundaries are at the transitional points where the velocity magnitude reduces to 20% of its maximum value in the inner and outer regions, respectively. The major and minor axes of the inner ellipse between the collar and the inner region are 7.9×10^6 m and 3.6×10^6 m, respectively. The major and minor axes of the outer ellipse are 13.7×10^6 m and 8.59×10^6 m, respectively. In an average sense, as marked in Fig. 26a, the collar can be further divided into the inner and outer rings by a dividing ellipse where the maximum velocity magnitude is locally attained. The major and minor axes of the dividing ellipse with the maximum velocity magnitude are 11.3×10^6 m and 6.44×10^6 m, respectively.

The local Cartesian coordinate system (x, y) at the center of the GRS and the orthogonal coordinates (n, s) along the dividing ellipse can be built, as shown in Fig. 26a, where s and n are the coordinates in the arc and transverse directions on the ellipse, respectively. The local transverse velocity profiles along the normal coordinate n at many cross-cuts are obtained from the velocity field, and then the mean transverse velocity profile across the
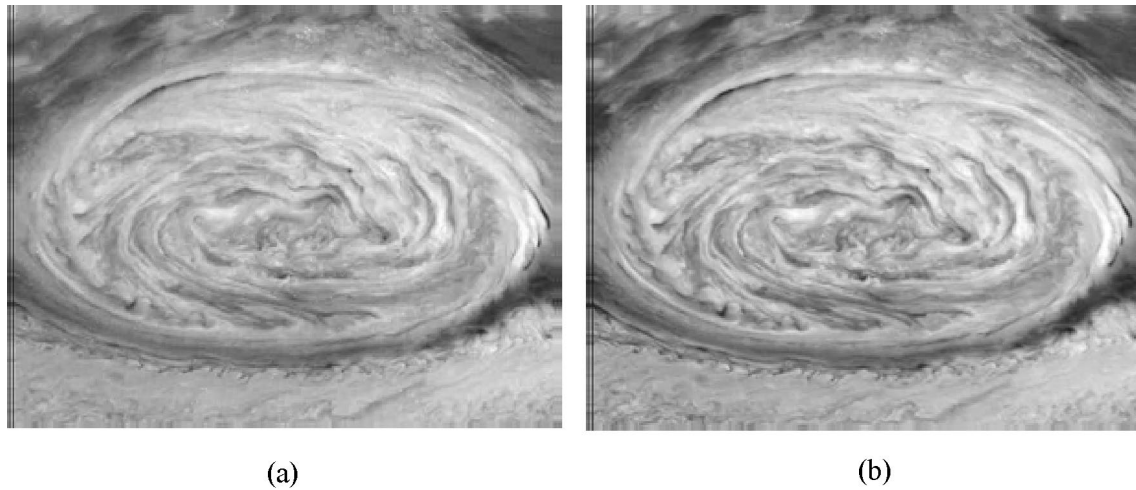
Fig. 23 Mosaics of the GRS taken by the Galileo spacecraft in 1996 (G1), where the time interval between the images (**a**, **b**) is 4320 s. From Liu et al. ([2012a](#), [b](#))
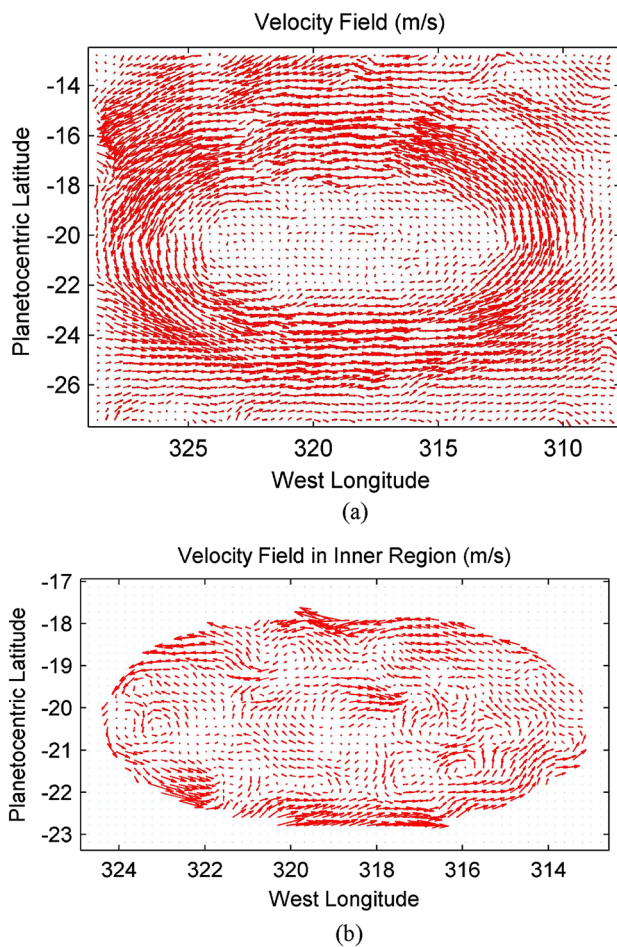

Fig. 24 Velocity fields of the GRS extracted by using OFM: **a** global view and **b** view of the inner region. Here the velocity fields are downsampled by 4 for clear illustration. From Liu et al. ([2012a](#), [b](#))

collar is calculated by averaging them along the elliptical coordinate s in a full cycle. As shown in Fig. 27, the measured transverse velocity profile across the collar obtained from the G1 images is reasonably described by the Bickley jet distribution $U(n)/U_{max} = \text{sech}^2\left(n/L_0\right)$ (Drazin and Reid [1981](#); McWilliams [2006](#)), where the mean maximum velocity is $U_{max} = 122$ m/s and the half-width of the Bickley jet is $L_0 = 3.22 \times 10^6$ m. The measured transverse velocity profile from the Galileo 2000 (G28) images are also plotted for comparison, where $U_{max} = 102$ m/s and $L_0 = 2 \times 10^6$ m. The inner and outer rings are essentially two shear layers of an elliptically circulating jet. The estimated shear-layer momentum thicknesses of the inner and outer rings for G1 are $\theta = 4.96 \times 10^5$ m and $\theta = 5.9 \times 10^5$ m, respectively.

The flow structures of the inner region of the GRS are intriguing. Previous velocity measurements using manual tracking and correlation methods indicate that the flow field in the inner region is somewhat incoherent and chaotic (Mitchell et al. [1981](#); Dowling and Ingersoll [1988](#); Sada et al. [1996](#); Choi et al. [2007](#)). On the other hand, as shown in Fig. 25a, the mean zonal velocity profiles suggest the persistent existence of the cyclonic (clockwise) rotation near the center in an average sense. However, the single zonal velocity profile averaged near the center itself is not sufficient to reveal the global pattern of this coherent structure and its dynamical significance.

To identify the major coherent structures in the inner region, the Gaussian-filtered velocity field is obtained, as shown in Fig. 26b, where a Gaussian filter with the standard deviation of 15 pixels is applied to the field of 231×302 velocity vectors. The non-filtered velocity field is shown in Fig. 30. The coarse-grained flow topology in the inner region is revealed, where four nodes denoted by
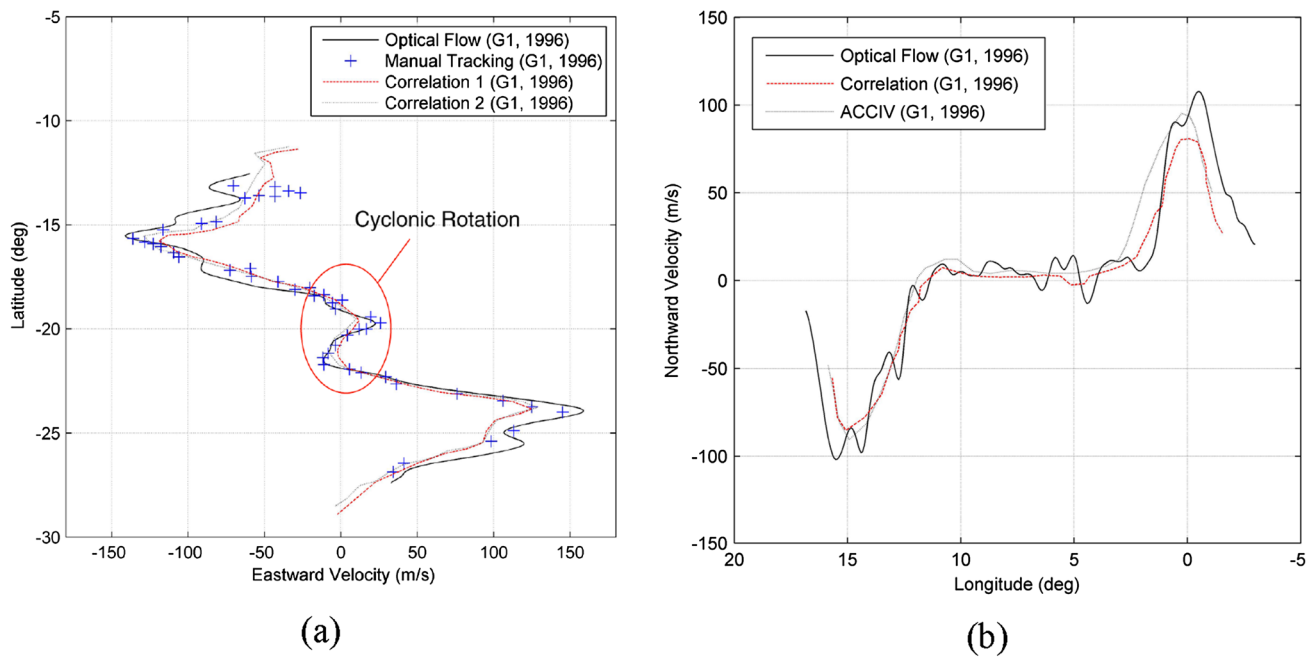
(a)

(b)

Fig. 25 The profiles of **a** the zonal and **b** meridional velocities averaged over a 2° strip along the minor and major axes across the GRS, respectively. The zonal data for comparison are obtained by Vasavada et al. (1998) using manual tracking and correlation method 1 and by Choi et al. (2007) using the correlation method 2. The meridional data for comparison are from Choi et al. (2007) and Asay-Davis et al. (2009) for ACCIV. From Liu et al. (2012a, b)

N_1, N_2, N_3 and N_4 are identified. The nodes N_2, N_3 and N_4 are sink nodes at which streamlines spiral inward anti-cyclonically. A simple topological constraint exists on the surface velocity field in the inner region of the GRS. A conservation law between the number of isolated critical points and the number of switch points in a singly connected region with a penetrable boundary on a surface is given by the Poincare–Bendixson index formula (Liu et al. 2011). Applying the Poincare–Bendixson index formula to a flow in a region enclosed by a penetrable boundary, Liu et al. (20,012) gave a topological rule for the inner region of the GRS, i.e., $\#N - \#S = 1$, where $\#N$ and $\#S$ are the numbers of nodes and saddles in the inner region, respectively. The topological rule is a mathematical constraint that must be satisfied for a velocity field. Clearly, the Gaussian-filtered velocity field in Fig. 26b satisfies this topological constraint since there are 4 nodes and 3 saddles. The topological constraint $\#N - \#S = 1$ imposes a necessary condition for the GRS. In fact, the non-filtered velocity field in Fig. (30) also satisfies this topological rule although there are many isolated critical points. A consequence is that there exists at least one node in the inner region of the GRS. This node in the inner region and the near-elliptical collar must coexist, and therefore this node must be long-lived. In Fig. 26(b), the cyclonic source node N_1 is a credible candidate for such a seed node associated with the cyclonic rotation near the center. This provides

a possible explanation for the persistent presence of the observed cyclonic rotation near the center of the GRS.

The topological analysis indicates the necessary presence of the node N_1. The physical origin of N_1 should be further discussed. As shown in the zoomed-in view in Fig. 26c, N_1 is a source since streamlines originated from it spiral outward cyclonically, inducing the eastward flow in the north of the node and the westward flow in the south of the node. As a result, the mean zonal velocity profile across this node exhibits the zigzag behavior as indicated in Fig. 25a. Since streamlines originating from N_1 spiral outward and the 2D velocity divergence is positive there, vertical flow toward the surface could exist beneath it. The connection between the cyclonic source node N_1 and the convection instability was discussed by Liu et al. (2012a, b). It was inferred that the convection instability could be responsible to the generation of the source node N_1. Further, the convection-induced stretching of the planetary vorticity could intensify the positive relative vorticity (clockwise rotation) at the source node N_1.

In addition to the above coarse-grained-structure analysis, a statistical analysis of fine flow structures in the collar and inner region can be made based on the non-filtered high-resolution velocity data obtained by OFM. Discrete vorticity-concentrated structures are found in the inner and outer rings of the collar, as shown in Fig. 28. To quantify these structures, the vorticity is transversely averaged along
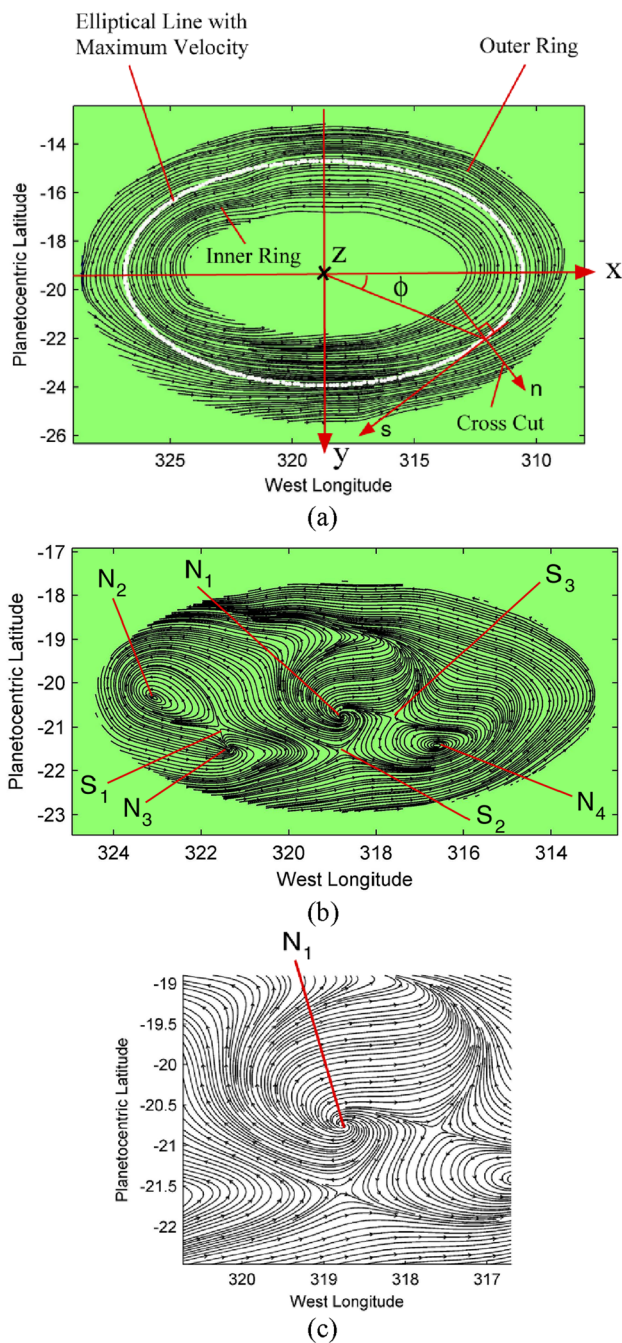
Fig. 26 Streamlines of the Gaussian-filtered velocity field of the GRS in **a** the collar, **b** the inner region and **c** the neighborhood of the cyclonic source node N_1. From Liu et al. (2012a, b)

Fig. 27 Mean transverse velocity profiles across the collar fitted by the Bickley jet distribution. From Liu et al. (2012a, b)

Fig. 28 Vorticity-concentrated structures in the collar of the GRS

the cross-cuts that are normal to the dividing ellipse at the middle of the collar. As shown in Fig. 29a, the cross-cut-averaged vorticity in the inner and outer rings of the collar exhibits a quasi-periodic behavior as a function of the polar angle or the arc length along the dividing ellipse in a local polar coordinate system located at the center of the GRS. The mean vorticity over a cycle of the polar angle
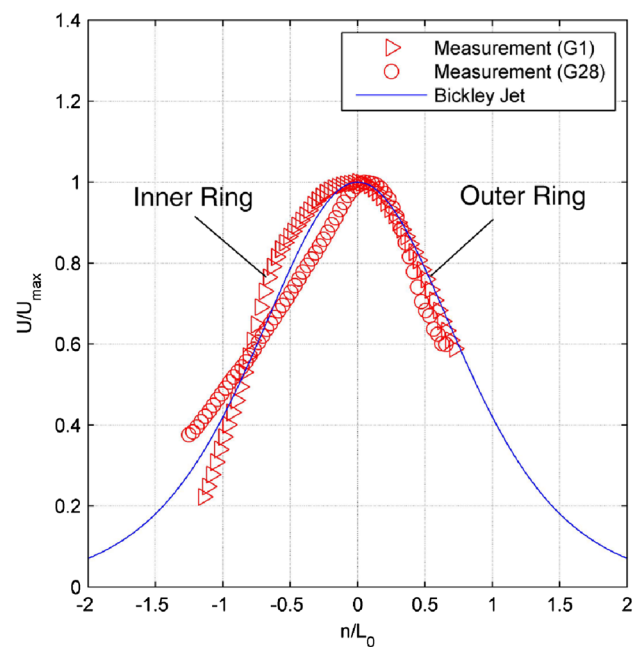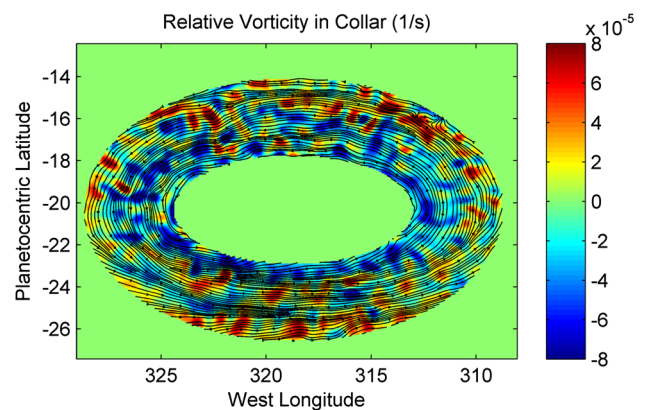
from 0 to 2π in the inner and outer rings are negative and positive, respectively. The negative mean value of the vorticity (counterclockwise or anticyclonic rotation) in the inner region indicates that most vortical structures have the negative vorticity there. The negative sign of the vorticity in the inner region is consistent with that of the inner ring of the high-speed collar. This implies that there is the relationship between the inner region and the inner ring of the high-speed collar. It will be indicated later that the kinetic energy in the inner region could be provided by the vortical structures generated in the inner ring of the high-speed collar.

Further, it is assumed that the vortical structures travel at an average convective velocity of $U_c = 0.5\, U_{max}$.
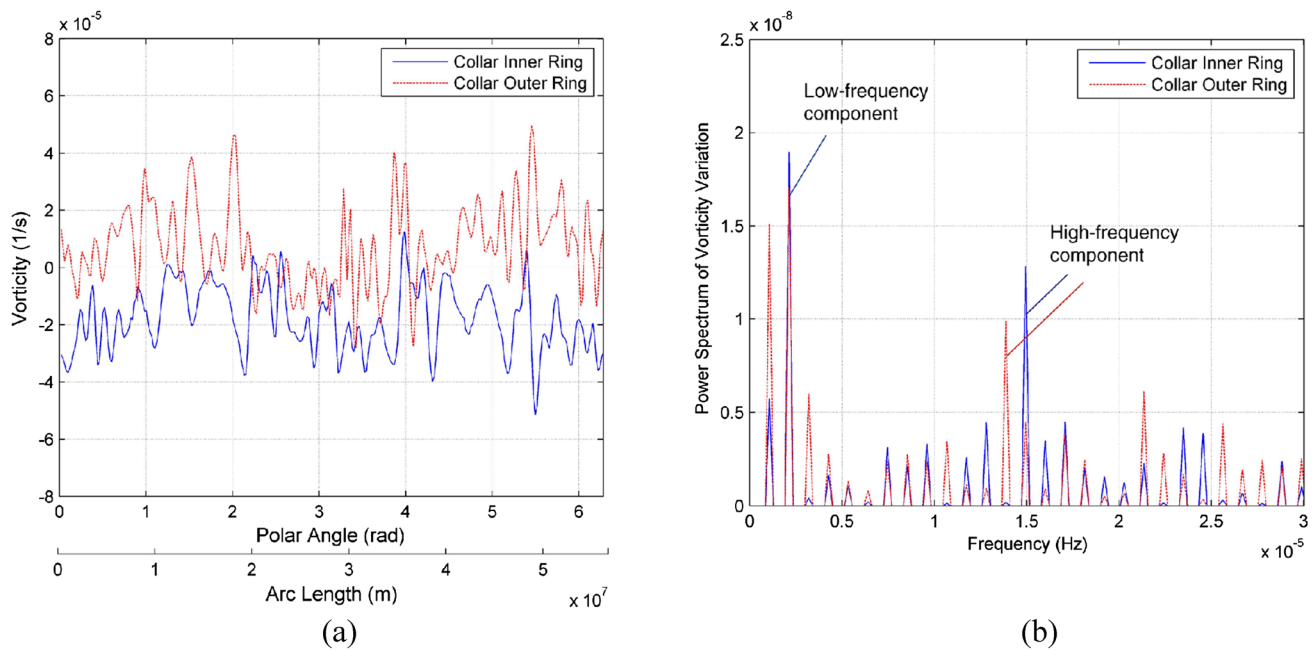
Fig. 29 **a** Cross-cut-averaged vorticity in collar's inner and outer rings of the GRS as a function of the polar angle or the arc length along the dividing ellipse, and **b** power spectrum of the vorticity fluctuation as the vortical structures travel along the dividing ellipse

This assumption has a rationale since the wave speed of the most amplifying even mode in the Bickley jet is just $c_r = 0.5\,U_{max}$ (Drazin and Reid 1981). Therefore, the time–space transformation $t = s/U_c$ is introduced, where s is the elliptical coordinate. A period in which the structures travel a full cycle along the collar is about $T = 2L/U_{max} = 9.37 \times 10^5$ s, where L is the arc length of the dividing ellipse. Therefore, the spatial variation of the vorticity can be converted to a time series of the vorticity fluctuation for a spectral analysis. Figure 29b shows the power spectra of the fluctuation of the cross-cut-averaged vorticity. The dominant high-frequency spectral peaks are found at 1.5×10^{-5} Hz ($k = 2.5 \times 10^{-7}$ m^{-1}) for the inner ring and 1.4×10^{-5} Hz ($k = 2.3 \times 10^{-7}$ m^{-1}) for the outer ring, where k indicates the corresponding wavenumber. For both the inner and outer rings, the dominant low-frequency peak is located at 2.1×10^{-6} Hz ($k = 3.5 \times 10^{-8}$ m^{-1}). The normalized wavenumbers of the high-frequency components in the inner and outer rings are $k L_0 = 0.8$ and $k L_0 = 0.75$, respectively, where the half-width is $L_0 = 3.22 \times 10^6$ m. In contrast, the normalized wavenumber of the dominant low-frequency component ($k = 3.5 \times 10^{-8}$ m^{-1}) is $k L_0 = 0.11$.

Naturally, a question arises: what are the possible mechanisms of generating the vortical structures in the collar? Several observational evidences are presented to shed insights into this problem. The measured normalized wavenumbers of the high-frequency components ($k L_0 = 0.8$ and $k L_0 = 0.75$) in the collar are close to $k L_0 = 0.9$ of the most

amplifying even mode predicted by the inviscid instability analysis for the Bickley jet (Drazin and Reid 1981; McWilliams 2006). The Bickley jet instability could be considered as a candidate mechanism. On the other hand, the normalized wavenumber of the low-frequency component ($k L_0 = 0.11$) is much lower than the most amplifying even mode in the Bickley jet. The most amplifying mode in a shear layer with the hyperbolic tangent velocity profile has the Strouhal numbers $St_\theta = f_s \theta / U_c = 0.032$ (Ho and Huerre 1984), where f_s is a frequency of a mode in a shear layer, θ is the shear-layer momentum thickness and $U_c = 0.5\,U_{max}$ is the median velocity of the shear layer. The wavelengths corresponding to $St_\theta = f_s \theta / U_c = 0.032$ for the inner and outer rings are $\lambda = 1.55 \times 10^7$ m and $\lambda = 1.84 \times 10^7$ m (wavenumbers are 6.45×10^{-8} m^{-1} and 5.43×10^{-8} m^{-1}), respectively, based on the measured momentum thicknesses. Therefore, the numbers of the vortical structures associated with the Kelvin–Helmholtz instability along the dividing ellipse with the total arc length of 5.5×10^7 m are 3.5 for the inner ring and 3 for the outer ring. Interestingly, this estimated number of the structures along the ellipse is close to 3 as predicted by Marcus (1993) for a circular vortex layer. Therefore, the Bickley jet instability and Kelvin–Helmholtz instability are probably responsible to the observed dominant high- and low-frequency components in the collar, respectively.

Figure 30 shows the detailed vorticity and 2D divergence fields in the inner region, revealing complex fine vortical structures. By counting the nodes in the inner region, it is
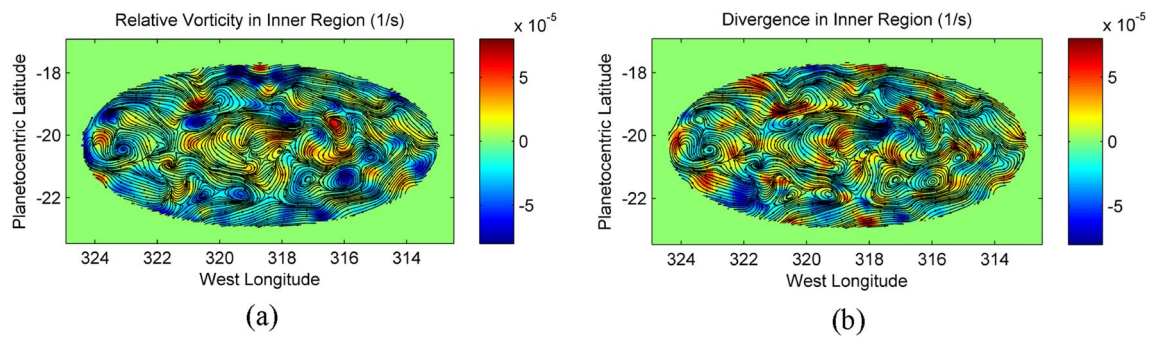
Fig. 30 Fine structures in the inner region of the GRS: **a** vorticity, and **b** 2D divergence

found that counterclockwise-rotating nodes with the negative relative vorticity prevail. Their sign of the relative vorticity is consistent with that of most vortical structures in the inner ring of the high-speed collar. As shown in Fig. 30b, the 2D divergence div(u) at these counterclockwise-rotating nodes is negative. Therefore, at these nodes, the vertical velocity gradient directing into the inside of Jupiter is positive according to the continuity equation. They are sink nodes where streamlines spiral inward. In addition, the second invariant of the velocity gradient tensor is distinctly positive at these nodes, indicating strong rotational motion and strongly spiral streamlines near these nodes. There are a few source nodes where the relative vorticity is positive and the vertical velocity gradient directing into the inside of Jupiter is negative. The second invariant at these source nodes is relatively small in comparison with most sink nodes, which indicates relatively weak rotational motion. A special attention is paid on the cyclonic (clockwise-spiraling) source node (N_1) near the center of the GRS since it is directly responsible to the cyclonic rotation motion there as indicated before.

In the inner region of the GRS, the kinetic energy spectrum of the velocity fluctuation is calculated. Figure 31 shows the kinetic energy spectrum in the inner region. The energy spectrum decays in the power law of k^{-3} in a wavenumber range of $3 \times 10^{-7} - 3 \times 10^{-6}\,\mathrm{m}^{-1}$. At smaller wavenumbers ($5 \times 10^{-8} - 3 \times 10^{-7}\,\mathrm{m}^{-1}$), the decaying slope of the energy spectrum is much smaller, approximately following the power law of k^{-1}. The kinetic energy spectra derived from the G1 and G28 images are shown for comparison. The theory of 2D homogenous isotropic turbulence predicts the kinetic energy spectrum $E(k) \propto k^{-3}$ in a forward enstrophy cascade inertial range (Kraichnan 1967; Batchelor 1969). The measured k^{-3}-range of the kinetic energy spectrum in the inner region is consistent with the 2D turbulence theory. In this sense, the flow in the inner region exhibits the characteristics of 2D turbulence at high wavenumbers. However, the short k^{-1}-range is observed at low wavenumbers, which
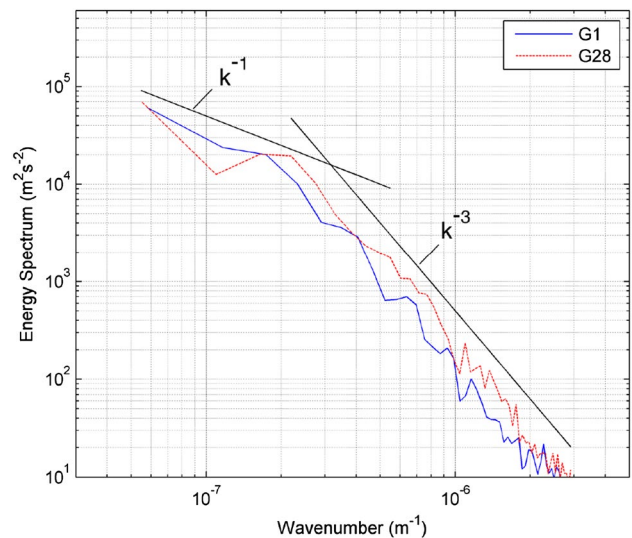

Fig. 31 Kinetic energy spectra of the flow in the inner region of the GRS

is different from the theoretical spectrum $E(k) \propto k^{-5/3}$ in the inverse energy cascade inertial range.

The transitional point between the k^{-3}- and k^{-1}-ranges is around $k = 3 \times 10^{-7}\,\mathrm{m}^{-1}$ that corresponds to a wavelength of 3,300 km. This length scale represents the typical scale of the vortical structures for energy injection into the inner region. The transitional wavenumber of about $k = 3 \times 10^{-7}\,\mathrm{m}^{-1}$ between the k^{-3}- and k^{-1}-ranges in the inner region is close to the dominant high-frequency component in the inner ring of the collar at the wavenumber $k = 2.5 \times 10^{-7}\,\mathrm{m}^{-1}$. This suggests that the vortical structures in the collar probably could pump the kinetic energy into turbulence in the inner region, acting as random forcing in the k^{-3} forward enstrophy cascade range. In the physical space, the vortical structures generated in the inner ring of the collar could drift into the inner region, entraining the kinetic energy from the high-speed collar into the inner

region. Indeed, as pointed out before, most vortices in the inner region have the negative relative vorticity (counter-clockwise or anticyclonic) just like those in the inner ring of the collar. Note that this wavelength at the transitional point is close to estimates of Jupiter's Rossby deformation radius by Cho et al. (2001) and Showman (2007) in their numerical simulations.

8 Typhoon Rai

Typhoon Rai (known as "Odette" in the Philippines) is the strongest storm of 2021, which made landfall on December 16, 2021, at 1:30 p.m. local time on Siargao Island in southeastern Philippines. The visible and infrared (IR) images of Rai were taken by the Japanese weather satellite Himawari-8. In this example, we focus on the IR images that are available in https://www.nrlmry.navy.mil/tcdat/tc2021/WP/WP282021/png_clean/Infrared-Gray/. A time sequence of 10 IR images of Rai taken at 11:49 in December 18, 2021, is processed using OFM, where the time interval between two sequential images is 10 min. Figure 32 shows the first pair of this sequence of IR images, where the high image intensity indicates low temperature. In the images in Fig. 32, the latitude is from 6° N to 18° N ($\phi_c = 6^o - 18^o$), and the longitude is from 106° E to 118° E ($\lambda = 106^o - 118^o$). For Earth with $R_e = 6378.137$ km and $R_p = 6356.7523$ km, the metric conversion factors along the coordinate curves (the latitude and longitude) on the surface in this observed region are approximately $r(\phi_g) = 6.2806 \times 10^6$ m/deg and $R(\phi_g) = 6.3374 \times 10^6$ m/deg. The conversion factors

in the images are approximately 948.07 m/pixel in the x-direction and 939.58 m/pixel in the y-direction.

The velocity fields of large-scale flow structures can be determined from a time sequence of IR images. To provide a solid foundation for the application of OFM to this problem, an optical flow equation can be derived by projecting the energy equation onto the image plane for IR satellite images of clouds in atmospheres. The IR image intensity I_T is proportional to temperature. Similar to Eq. (8), the optical flow equation for IR images can be written as $\partial I_T / \partial t + \nabla \cdot (I_T \boldsymbol{u}) = f(x_1, x_2)$, where the optical flow is $\boldsymbol{u} = (u_1, u_2) = \gamma \langle \boldsymbol{U}_{12} \rangle_T$, $\langle \boldsymbol{U}_{12} \rangle_T$ is the light-path-averaged velocity through a thermal layer with detected IR radiation [see Eq. (9)], and $f(x_1, x_2)$ is a source term. Therefore, for IR images, the optical flow can be determined by solving the Euler–Lagrange equation Eq. (11).

Nine snapshot velocity fields in the top layer of Rai are obtained from the sequence of IR images using OFM. Before optical flow computation, these images are downsampled by 4 and smoothed by using a Gaussian filter with a standard deviation of 2 pixels. An extracted velocity field contains 350×350 velocity vectors. Figure 33a shows a typical snapshot velocity field extracted from the image pair in Fig. 32. This velocity field relative to the ground is decomposed into the counterclockwise spiral rotational motion around the eye (the center) of the typhoon and the overall translational motion. As shown in Fig. 33b, the rotational velocity field is obtained by subtracting the velocity of the eye of Rai. Figure 34 shows the time-averaged velocity vectors and streamlines of Rai superposed on the velocity magnitude field normalized by the maximum velocity magnitude, where the (x, y) coordinates are normalized by the radial
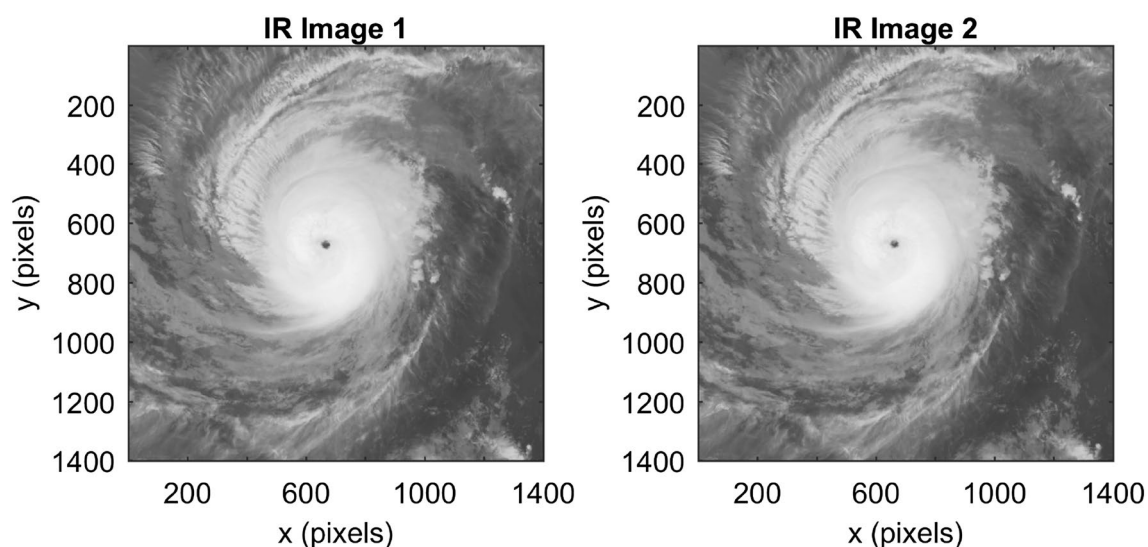

Fig. 32 A typical pair of IR images of Typhoon Rai taken by the satellite Himawari-8 on December 18, 2021, where the time interval between the two images is 10 min
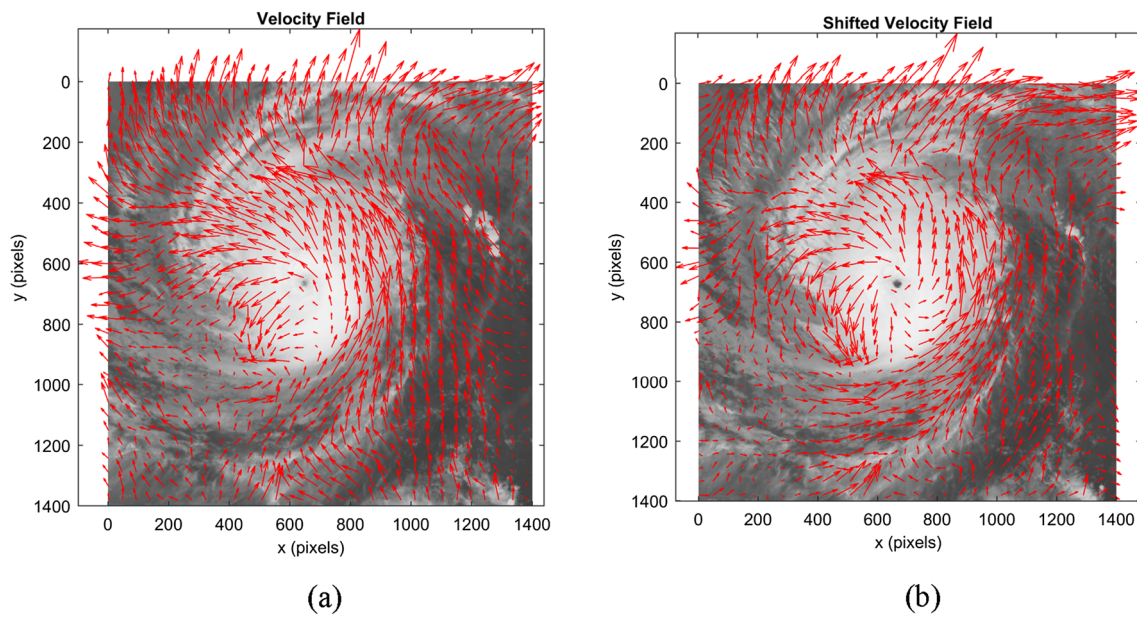
Fig. 33 The snapshot velocity field extracted from a typical pair of IR images of Typhoon Rai in Fig. 32 using OFM: **a** velocity field, and **b** shifted velocity based on the velocity of the eye of Rai
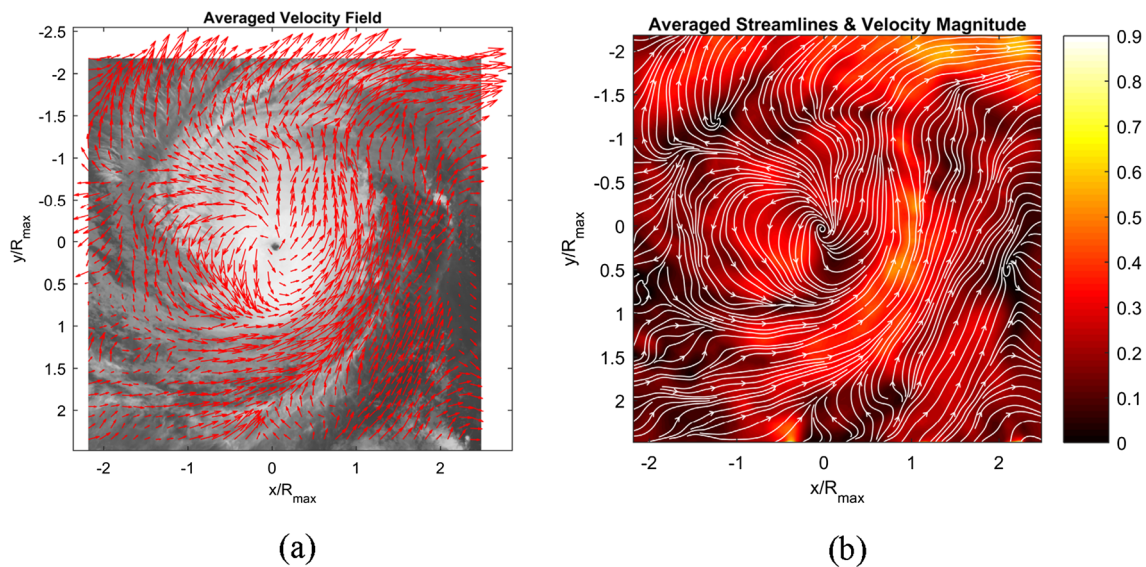

Fig. 34 The time-averaged velocity field of Typhoon Rai: **a** velocity vectors, and **b** streamlines superposed on the normalized velocity magnitude field

location R_{max} from the eye of Rai at which the maximum velocity magnitude is attained. The measured value of R_{max} is 284 km. The maximum wind velocity magnitude in the observation domain relative to the ground is approximately 25 m/s (48.6 knots).

Since the top-layer flow of Rai is counterclockwisely spiral outwardly, the velocity $\boldsymbol{u}$ is decomposed into the circumferential and radial components (u_θ, u_r) in a polar coordinate system (θ, r), where u_θ is positive when the flow is counterclockwise and u_r is positive when the flow moves outward from the center. The time-averaged circumferential and radial velocity components are $\langle u_\theta \rangle_t$ and $\langle u_r \rangle_t$, respectively, where $\langle \rangle_t$ denotes the time-averaging operator. Further, the azimuthally averaged velocity comments are $\left\langle \langle u_\theta \rangle_t \right\rangle_\theta$ and $\left\langle \langle u_r \rangle_t \right\rangle_\theta$, where $\langle \rangle_\theta$ is the averaging operator in the polar angle $\theta \in [0, 2\pi]$. Figure 35 shows
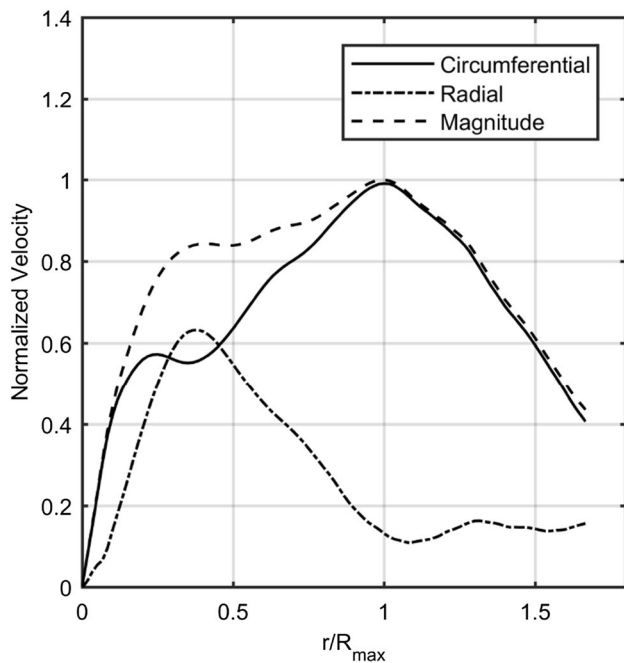
Fig. 35 The azimuthally averaged velocity profiles of Typhoon Rai normalized by the maximum velocity magnitude, including the circumferential component, radial component, and magnitude
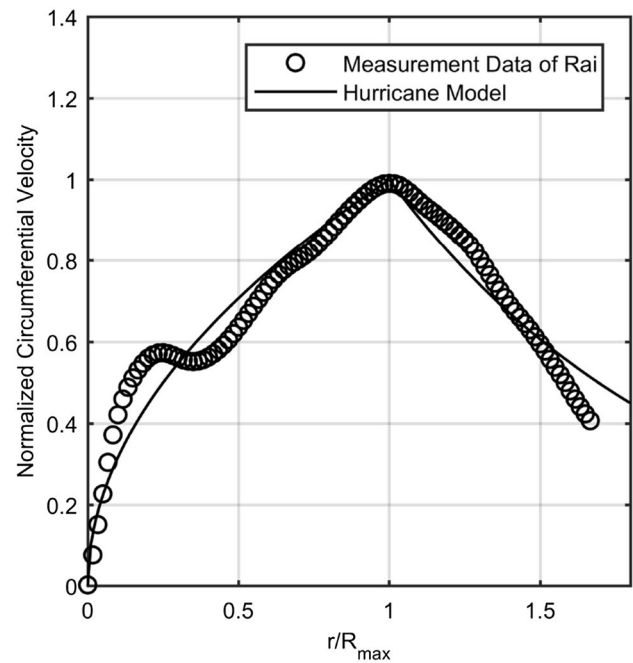

Fig. 36 The azimuthally averaged circumferential velocity profile of Typhoon Rai normalized by its maximum magnitude in comparison with the Hurricane model

the profiles of $\left\langle \langle u_\theta \rangle_t \right\rangle_\theta$, $\left\langle \langle u_r \rangle_t \right\rangle_\theta$ and $\left\langle \langle |\boldsymbol{u}| \rangle_t \right\rangle_\theta$ normalized by the maximum velocity magnitude.

The empirical hurricane models were proposed to fit the wind velocity data obtained by reconnaissance aircraft flying through hurricanes (Willoughry et al. 2006). To describe the circumferential velocity profile of a symmetrical circular vortex, the simplest model is a two-piece function defined as

$$
\bar{u}_\theta =
\begin{cases}
\bar{r}^n & 0 \leq \bar{r} \leq 1 \\
\exp\left(-(\bar{r}-1)/\overline{X}_1\right) & \bar{r} > 1
\end{cases}, \tag{12}
$$

where the normalized velocity is $\bar{u}_\theta = u_\theta / \max\left(u_\theta\right)$, the normalized radial coordinate is $\bar{r} = r/R_{\max}$, n is an exponent of the power law for the interior region, and $\overline{X}_1 = X_1/R_{\max}$ represents the relative size of the outer region where the velocity decays exponentially. An empirical transition function could be used to overlap the two regions smoothly. For simplicity, Eq. (12) is used to fit the data in this case without applying a transitional function. Figure 36 shows the measured circumferential velocity profile of Rai in comparison with the two-piece hurricane model with $n = 0.5$ and $\overline{X}_1 = 1$. This model approximately fits the measurement data. The parameters n and $\overline{X}_1$ are, to some extent, correlated with the maximum circumferential velocity. For Typhoon Rai with the measured maximum circumferential velocity of $\max\left(u_\theta\right) \approx 25$ m/s, the selected parameters of $n = 0.5$ and

$\overline{X}_1 = 1$ in this model are consistent with the data collected in many reconnaissance aircraft flight sorties through hurricanes (see Fig. 6 in Willoughry et al. 2006).

9 Conclusions

Cloud tracking is a key method to extract velocity fields of atmospheres of planets (for example Jupiter, Saturn and Earth) from cloud images obtained in ground-based and space-based observations such that the physics of planets can be explored. From a standpoint of flow measurements, cloud tracking is a special form of global flow diagnostics based on natural flow visualizations in planet's atmospheres where clouds act as passive tracers. Therefore, this topic would be of interest to experimental fluid dynamicists. Manual tracking is the simplest method by visually identifying common cloud features in sequence and marking their coordinates, which has been used to provide valuable velocity dataset to study planetary flow structures particularly Jupiter's Great Red Spot (GRS), White Ovals (WOs) and zonal jet streams. However, manual tracking gives velocity fields at irregularly distributed and sparse locations, and sub-pixel accuracy in determining the displacement vectors cannot be obtained. Correlation image velocimetry (CIV) is an automated method that finds matching features by correlating small windows of pixels in two cloud images, which

is an adapted version of PIV for continuous cloud patterns. For cloud images lacking distinct trackable features, spatial cross-correlation calculated between continuous patterns in windows has a small value, which could generate many spurious velocity vectors that must be removed manually or automatically. The optical flow method (OFM) is developed by projecting the transport equation of scalar tracers in the three-dimensional object space onto the image plane to model an imaging process in flow visualizations. In principle, as a differential method, OFM is particularly suitable for extraction of small displacements from cloud images at a spatial resolution of one vector per pixel. The accuracy of OFM is examined based on simulated cloud images of the GRS. It is found that OFM performs better in comparison with other cloud-tracking algorithms. The capability of OFM is demonstrated in its application to extract the high-resolution velocity field from the Galileo 1996 images of the GRS in comparison with the previous results obtained using manual tracking and CIV. Furthermore, OFM is used to extract the velocity fields of Typhoon Rai from satellite infrared images.

References

Antuñano A, del Río-Gaztelurrutia T, Sánchez-Lavega A, Hueso R (2015) Dynamics of Saturn's polar regions. J Geophys Res Planets 120:155–176. https://doi.org/10.1002/2014JE004709

Antuñano A, del Río-Gaztelurrutia T, Sánchez-Lavega A, Rodriguez-Aseguinolaza J (2018) Cloud morphology and dynamics in Saturn's northern polar region. Icarus 299:117–132. https://doi.org/10.1016/j.icarus.2017.07.017

Asay-Davis X, Marcus P, Wong W, de Pater L (2009) Jupiter's shrinking Great Red Spot and steady Oval BA: velocity measurements with the 'Advection Corrected Correlation Image Velocimetry' automated cloud-tracking method. Icarus 203:164. https://doi.org/10.1016/j.icarus.2009.05.001

Auroux D, Fehrenbach J (2011) Identification of velocity fields for geophysical fluids from a sequence of images. Exp Fluids 50:313–328. https://doi.org/10.1007/s00348-010-0926-9

Baines K, Momary T, Temma T, Buratti B, Roos-Serote M, Showman A, Brown R, Clark R, Nicholson P, Atreya S, Graham J., Marquez E (2007) The structure of Saturn's poles determined by Cassini/VIMS: Constraints on winds and horizontal and vertical cloud distributions. American Astronomical Society, DPS meeting #39, id.9.02; Bulletin of the American Astronomical Society, 39:423.

Baines K, Momary T, Fletcher L, Showman A, Roos-Serote M, Brown R, Buratti B, Clark R, Nicholson P (2009) Saturn's north polar cyclone and hexagon at depth revealed by Cassini/

VIMS. Planet Sp Sci 57:1671–1681. https://doi.org/10.1016/j.pss.2009.06.026

Batchelor GK (1969) Computation of the energy spectrum in homogenous two-dimensional turbulence. Phys Fluids Suppl II 12:233

Bucci LR, O'Handley C, Emmitt GD, Zhang JA, Ryan K, Atlas R (2018) Validation of an airborne Doppler wind lidar in tropical cyclones. Sensors 18:4288. https://doi.org/10.3390/s18124288

Cai S, Mémin E, Dérian P, Xu C (2018) Motion estimation under location uncertainty for turbulent fluid flows. Exp Fluids 59(1):1–17. https://doi.org/10.1007/s00348-017-2458-z

Cheng AF, Simon-Miller AA, Weaver HA, Baines KH, Orton GS, Yanamandra-Fisher PA, Mousis O, Pantin E, Vanzi L, Fletcher LN, Spencer JR, Stern SA, Clarke JT, Mutchler MJ, Noll KS (2008) Changing characteristics of Jupiter's Little Red SPOT. Astron J 135:2446–2452. https://doi.org/10.1088/0004-6256/135/6/2446

Cho JY-K, de la Torre Juarez M, Dritschel IA, DG, (2001) A high-resolution, three-dimensional model of Jupiter's Great Red Spot. J Geophys Res 106(E3):5099–5105. https://doi.org/10.1029/2000JE001287

Choi D, Banfield D, Gierasch P, Showman A (2007) Velocity and vorticity measurements of Jupiter's Great Red Spot using automated cloud feature tracking. Icarus 188:35. https://doi.org/10.1016/j.icarus.2006.10.037

Choi D, Showman A, Brown R (2009) Cloud features and zonal wind measurements of Saturn's atmosphere as observed by Cassini/VIMS. J Geophys Res 114:E04007. https://doi.org/10.1029/2008JE003254

Choi D, Showman AP, Vasavada AR (2010) The evolving flow of Jupiter's White Ovals and adjacent cyclones. Icarus 207:359–372. https://doi.org/10.1016/j.icarus.2009.10.013

Cui L, Shi L, Yin G, Yu W, Yu X, Liu J (2013) Application of satellite cloud imagery in track analysis of tropical cyclones. Trop Cyclone Rese Rev 2(4):222–232. https://doi.org/10.6057/2013TCRR04.04

Dowling TE (1995) Dynamics of jovian atmospheres. Annu Rev Fluid Mech 27:293

Dowling TE, Ingersoll AP (1988) Potential vorticity and layer thickness variation in the flow around Jupiter's Great Red Spot and white Oval BC. J Atmos Sci 45(8):1380–1396. https://doi.org/10.1175/1520-0469(1988)045%3c1380:PVALTV%3e2.0.CO;2

Drazin PG, Reid WH (1981) Hydrodynamic stability. Cambridge University Press, Cambridge, pp 233–237. https://doi.org/10.1017/CBO9780511616938

Dyudina U, Ingersoll A, Ewald S, Vasavada A, West R, Baines K, Momary T, Del Genio A, Barbara J, Porco C, Achterberg R, Flasar F, Simon-Miller A, Fletcher L (2009) Saturn's south polar vortex compared to other large vortices in the solar system. Icarus 202:240–248. https://doi.org/10.1016/j.icarus.2009.02.014

Emanuel KA (1991) The theory of hurricanes. Annu Rev Fluid Mech 23:179–196. https://doi.org/10.1146/annurev.fl.23.010191.001143

Fincham A, Delerce G (2000) Advanced optimization of correlation imaging velocimetry algorithms. Exp Fluids 29:S013–S022. https://doi.org/10.1007/s003480070003

Fincham A, Spedding G (1997) Low cost, high resolution DPIV for measurement of turbulent flow. Exp Fluids 23:449–462. https://doi.org/10.1007/s003480050135

Fletcher L, Irwin P, Orton Tenby N, Achterberg R, Bjoraker G, Read P, Simon-Miller A, Howett C, de Kok R, Bolwes N, Calcutt S, Hesman B, Flasar F (2008) Temperature and composition of Saturn's polar hot spots and hexagon. Science 319(5859):70–82. https://doi.org/10.1126/science.1149514

Garcia-Melendo ES, Lanchez-Lavega A (2001) A Study of the Stability of Jovian Zonal Winds from HST Images: 1995–2000. Icarus 152:316–330. https://doi.org/10.1006/icar.2001.6646

Godfrey D (1988) A hexagonal feature around Saturn's north pole. Icarus 76:335–356. https://doi.org/10.1016/0019-1035(88)90075-9

Hansen CJ, Caplinger MA, Ingersoll A, Ravine MA, Jensen E, Bolton S, Orton G (2017) Junocam: Juno's outreach camera. Sp Sci Rev 213:475–506. https://doi.org/10.1007/s11214-014-0079-x

Héas P, Mémin E (2008) Three-dimensional motion estimation of atmospheric layers from image sequences. IEEE Trans Geosci Remote Sens 46(8):2385–2396. https://doi.org/10.1109/TGRS.2008.918167

Héas P, Mémin E, Papadakis N, Szantai A (2007) Layered estimation of atmospheric mesoscale dynamics from satellite imagery. IEEE Trans Geosci Remote Sens 45(12):4087–4104. https://doi.org/10.1109/TGRS.2007.906156

Héas P, Mémin E, Heitz D, Mininni PD (2012) Power laws and inverse motion modelling: application to turbulence measurements from satellite images. Tellus A Dyn Meteorol Oceanogr 64:1. https://doi.org/10.3402/tellusa.v64i0.10962

Heitz D, Memin E, Schnorr C (2010) Variational fluid flow measurements from image sequences: synopsis and perspectives. Exp Fluids 48:369–393. https://doi.org/10.1007/s00348-009-0778-3

Ho C-M, Huerre P (1984) Perturbed free shear layers. Ann Rev Fluid Mech 16:365–425. https://doi.org/10.1146/annurev.fl.16.010184.002053

Holton J, Hakim G (2013) Introduction to dynamic meteorology, 5th edn. Elsevier, New York. https://doi.org/10.1016/B978-0-12-384866-6.00039-8

Hooke R (1665) A spot on one of the belts of Jupiter. Philos Trans R Soc 1(1): 3. https://doi.org/10.1098/rstl.1665.0005.

Horn B, Schunck B (1981) Determining optical flow. Artif Intell 17(1–3):185–204. https://doi.org/10.1016/0004-3702(81)90024-2

Hueso R, Legarreta J, Garcia-Melendo E, Sanchez-Lavega A, Perez-Hoyos S (2009) The jovian anticyclone BA. II. Circulation and interaction with the zonal jets. Icarus 203(2):499–515. https://doi.org/10.1016/j.icarus.2009.05.004

Hueso R, Legarreta J, Rojas JF, Peralta J, Pérez-Hoyos S, del Río GT, Sánchez-Lavega A (2010) The planetary laboratory for image analysis (PLIA). Earth Moon Planets Adv Sp Res 46:1120–1138. https://doi.org/10.1016/j.asr.2010.05.016

Ingersoll AP (2020) Cassini exploration of the planet Saturn: a comprehensive review. Sp Sci Rev 216:122. https://doi.org/10.1007/s11214-020-00751-1

Ingersoll AP, Dowling TE, Gierasch PJ, Orton GS, Read PL, Sánchez-Lavega A, Showman AP, Simon-Miller AA, Vasavada AR (2004) Dynamics of Jupiter's atmosphere. Chapter 6. In: Jupiter: the planet, satellites, and magnetosphere. Bagenal F, Dowling TE, McKinnon WB (eds) Cambridge University Press, p 105

Janssen V (2009) Understanding coordinate systems, datums and transformations in Australia. In: Ostendorf B, Baldock P, Bruce D, Burdett M, Corcoran P (eds) Proceedings of the Surveying & Spatial Sciences Institute Biennial International Conference, Adelaide 2009, Surveying & Spatial Sciences Institute, pp 697–715.

Johnson PE, Morales-Juberías R, Simon AA, Gaulme P, Wong MH, Cosentino RG (2018) Longitudinal variability in Jupiter's zonal winds derived from multi-wavelength HST observations. Planet Sp Sci 155:2–11. https://doi.org/10.1016/j.pss.2018.01.004

Kouyama T, Imamura T, Nakamura M, Satoh T, Futaana Y (2012) Horizontal structure of planetary-scale waves at the cloud top of Venus deduced from Galileo SSI images with an improved cloud-tracking technique. Planet Sp Sci 60:207–216. https://doi.org/10.1016/j.pss.2011.08.008

Kouyama T, Imamura T, Nakamura M, Satoh T, Futaana Y (2013) Long-term variation in the cloud-tracked zonal velocities at the cloud top of Venus deduced from Venus Express VMC images. J Geophys Res Planets 118:37–46. https://doi.org/10.1029/2011JE004013

Kraichnan RH (1967) Inertial ranges in two-dimensional turbulence. Phys Fluids 10:1417–1423

Leese JA, Novak CS, Clark BB (1971) An automated technique for obtaining cloud motion from geosynchronous satellite data using cross correlation. J Appl Meteorol Climatol 10(1):118–132. https://doi.org/10.1175/1520-0450(1971)010%3c0118:AATFOC%3e2.0.CO;2

Legarreta J, Sánchez-Lavega A (2005) Jupiter's cyclones and anticyclones vorticity from Voyager and Galileo images. Icarus 174:178–191. https://doi.org/10.1016/j.icarus.2004.10.006

Limaye SS (1986) Jupiter—new estimates of the mean zonal flow at the cloud level. Icarus 65:335–352. https://doi.org/10.1016/0019-1035(86)90142-9

Lindal GF, Sweetnam DN, Eshleman VR (1985) The atmosphere of Saturn—an analysis of the Voyager radio occultation measurements. Astron J 90:1136–1146. https://doi.org/10.1086/113820

Liu T (2017) OpenOpticalFlow: an open source program for extraction of velocity fields from flow visualization images. J Open Res Softw 5:29. https://doi.org/10.5334/jors.168

Liu T, Salazar DM (2021) OpenOpticalFlow_PIV: an open source program integrating optical flow method with cross-correlation method for particle image velocimetry. J Open Res Softw 9(1):3. https://doi.org/10.5334/jors.326

Liu T, Shen L (2008) Fluid flow and optical flow. J Fluid Mech 614:253. https://doi.org/10.1017/S0022112008003273

Liu T, Woodiga S, Ma T (2011) Skin friction topology in a region enclosed by penetrable boundary. Exp Fluids 51:1549. https://doi.org/10.1007/s00348-011-1171-6

Liu T, Wang B, Choi D (2012a) Flow structures of Jupiter's Great Red Spot extracted by using optical flow method. Phys Fluids 24:096601–096613. https://doi.org/10.1063/1.4752227

Liu T, Burner AW, Jones T, Barrow D (2012b) Photogrammetric techniques for aerospace applications. Prog Aerosp Sci 54:1–58. https://doi.org/10.1016/j.paerosci.2012.03.002

Liu T, Merat A, Makhmalbaf M, Fajardo C, Merati P (2015) Comparison between optical flow and cross-correlation methods for extraction of velocity fields from particle images. Exp Fluids 56:166–189. https://doi.org/10.1007/s00348-015-2036-1

Liu T, Sanyanagi KM, Brueshaber S, Ingersoll AP, Dyudina UA, Ewald SP (2019) Saturn's north polar vortex structure extracted from cloud images by the optical flow method. J Geophys Res Planets 124(11):3041–3062. https://doi.org/10.1029/2019JE005974

Liu T, Salazar D, Fagehi H, Ghazwani H, Montefort MJP (2020) Hybrid Optical-flow-cross-correlation method for particle image velocimetry. J Fluids Eng 142(5):05450. https://doi.org/10.1115/1.4045572

Marcus P (1993) Jupiter's Great Red Spot and other vortices. Annu Rev Astron Astrophys. https://doi.org/10.1146/annurev.aa.31.090193.002515

McWilliams JC (2006) Fundamentals of geophysical fluid dynamics. Cambridge University Press, Cambridge, pp 78–80. https://doi.org/10.2277/052185637X

Meissner T, Ricciardulli L, Andrew Manaster A (2021) Tropical cyclone wind speeds from WindSat, AMSR and SMAP: algorithm development and testing. Remote Sens 13:1641. https://doi.org/10.3390/rs13091641

Menzel WP (2001) Cloud tracking with satellite imagery: from the pioneering work of Ted Fujita to the present. Bull Am Meteorol Soc 82(1):33–48. https://doi.org/10.1175/1520-0477(2001)082%3c0033:CTWSIF%3e2.3.CO;2

Merrill RT (1988) Characteristics of the upper-tropospheric environmental flow around hurricanes. J Atmos Sci 45(11):1665–1677. https://doi.org/10.1175/1520-0469(1988)045%3c1665:COTUTE%3e2.0.CO;2

Mitchell JL, Beebe RF, Ingersoll AP, Carneau GW (1981) Flow fields with Jupiter's Great Red Spot and white oval BC. J Geophys Res 86(A10):8751–8757. https://doi.org/10.1029/JA086iA10p08751

Ottenbacher A, Tomassini M, Holmlund K, Schmetz J (1997) Low-level cloud motion winds from Meteosat high-resolution visible imagery. Weather Forecast 12(1):175–184. https://doi.org/10.1175/1520-0434(1997)012%3c0175:LLCMWF%3e2.0.CO;2

Ravela S, Marshall J, Hill C, Wong A, Stransky S (2010) (2010) A real-time observatory for laboratory simulation of planetary flows. Exp Fluids 48:915–925. https://doi.org/10.1007/s00348-009-0752-0

Read P, Gierasch P, Conrath B, Yamazaki Y (2005) 3d balanced winds and dynamics in Jupiter's atmosphere from combined imaging and infrared observations. Adv Sp Res 36:2187–2193. https://doi.org/10.1016/j.asr.2005.04.026

Read P, Gierasch PI, Conrath BJ (2006) Mapping potential-vorticity dynamics on Jupiter. II: the Great Red Spot from Voyager 1 and 2 data. Q J R Meteorol Soc 132:1605–1625. https://doi.org/10.1256/qj.05.35

Rossow WB, del Genio AD, Eichler T (1990) Cloud-tracked winds from Pioneer Venus OCPP images. J Atmos Sci 47:2053–2084. https://doi.org/10.1175/1520-0469(1990)047%3c2053:CTWFVO%3e2.0.CO;2

Sada F, Beebe RF, Conrath BJ (1996) Comparison of the surface and dynamics of Jupiter's Great Red Spot between the Voyager 1 and 2 encounters. Icarus 119:311–335. https://doi.org/10.1006/icar.1996.0022

Sánchez-Lavega A, Rojas JF, Sada PV (2000) Saturn's zonal winds at cloud level. Icarus 147:405–420. https://doi.org/10.1006/icar.2000.6449

Sánchez-Lavega A, Hueso R, Pérez-Hoyos S, Rojas J (2006) A strong vortex in Saturn's south pole. Icarus 184:524–531. https://doi.org/10.1016/j.icarus.2006.05.020

Sayanagi KM, Dyudina UA, Ewald SP, Muro GD, Ingersoll AP, West RA, Porco CC (2011) Dynamics of Saturn's great storm of 2010–2011 from Cassini ISS and RPWS. Icarus 223:460–478. https://doi.org/10.1016/j.icarus.2012.12.013

Sayanagi K, Dyudina U, Ewald S, Ingersoll A (2017) Cassini ISS observation of Saturn's north polar vortex and comparison to the south polar vortex. Icarus 285:68–82. https://doi.org/10.1016/j.icarus.2016.12.011

Sayanagi KM, Baines KH, Dyudina UA, Fletcher LN, Sanchez-Lavega A, West RA (2019) Saturn's polar atmosphere. In: Baines KH, Flasar FM, Krupp N, Stallard T (eds) Saturn in the 21st century. Cambridge University Press, Cambridge. https://doi.org/10.1017/9781316227220.012

Seidelmann PK, Abalakin VK, Bursa M et al (2002) Report of the IAU IAG COSPAR working group on cartographic coordinates and rotational elements of the planets and satellites. Celest Mech Dyn Astron 82:83–110. https://doi.org/10.1023/A:1013939327465

Shetty S, Asay-Davis XS, Macus PS (2007) On the interaction of Jupiter's Great Red Spot and zonal jet streams. J Atmos Sci 64:4432–4444. https://doi.org/10.1175/2007JAS2097.1

Showman AP (2007) Numerical simulations of forced shallow-water turbulence: effects of moist convection on the large-scale circulation of Jupiter and Saturn. J Atmos Sci 64:3132–3157. https://doi.org/10.1175/JAS4007.1

Simon AA, Tabataba-Vakili F, Cosentino R, Beebe RE, Wong MH, Orton GS (2018) Historical and contemporary trends in the size, drift, and color of Jupiter's Great Red Spot. Astronomical J 155:151. https://doi.org/10.3847/1538-3881/aaae01 (**13pp**)

Simon-Miller AA, Gierasch PJ (2010) On the long-term variability of Jupiter's winds and brightness as observed from Hubble. Icarus 210:258–269. https://doi.org/10.1016/j.icarus.2010.06.020

Simon-Miller AA, Gierasch PJ, Beebe RF, Conrath B, Flasar FM, Achterberg R, the Cassini CIR Team (2002) New observational results concerning Jupiter's Great Red Spot. Icarus 158:249–266. https://doi.org/10.1006/icar.2002.6867

Simon-Miller AA, Conrath BJ, Gierasch PJ, Orton GS, Achterberg RK, Flasar FM, Fisher BM (2006) Jupiter's atmospheric temperatures: from Voyager IRIS to Cassini CIRS. Icarus 180:98–112. https://doi.org/10.1016/j.icarus.2005.07.019

Simon-Miller AA, Poston BW, Orton GS, Fisher B (2007) Wind variations in Jupiter's equatorial atmosphere: a QQO counterpart? Icarus 186:192–203. https://doi.org/10.1016/j.icarus.2006.08.009

Smith R, Vogl S (2003) A simple model of the hurricane boundary layer. Q J R Meteorol Soc 129:1007–1027. https://doi.org/10.1002/qj.216

Studwell A, Li L, Jiang X, Baines KH, Fry PM, Momary TW, Dyudina UA (2018) Saturn's global zonal winds explored by Cassini/VIMS 5-micron images. Geophys Res Lett 45(14):6823–6831. https://doi.org/10.1029/2018GL078139

Sussman MG, Chanover NJ, Simon-Miller AA, Vasavada AR, Beebe RF (2010) Analysis of Jupiter's Oval BA: a streamlined approach. Icarus 210:202–210. https://doi.org/10.1016/j.icarus.2010.06.044

Thielicke W, Stamhuis EJ (2014) PIVlab—towards user-friendly, affordable and accurate digital particle image velocimetry in MATLAB. J Open Res Softw 2(1):e30. https://doi.org/10.5334/jors.bl

Toigo A, Gierasch PJ, Smith MD (1994) High resolution cloud feature tracking on Venus by Galileo. Icarus 109:318–336. https://doi.org/10.1006/icar.1994.1097

Tokumaru PT, Dimotakis PE (1995) Image correlation velocimetry. Exp Fluids 19:1–15. https://doi.org/10.1007/BF00192228

Torge W (2001) Geodesy, 3rd edn. de Gruyter, Berlin. https://doi.org/10.1515/9783110879957

Tuttle J, Gall R (1999) A single-radar technique for estimating the winds in tropical cyclones. Bull Am Meteorol Soc 80(4):653–668. https://doi.org/10.1175/1520-0477(1999)080%3c0653:ASRTFE%3e2.0.CO;2

Uhlhorn EW, Black PG (2003) Verification of remotely sensed sea surface winds in hurricanes. J Atmos Ocean Technol 20:99–116. https://doi.org/10.1175/1520-0426(2003)020%3c0099:VORSSS%3e2.0.CO;2

Vasavada A, Showman AP (2005) Jovian atmospheric dynamics: an update after Galileo and Cassini. Rep Prog Phys 68:1935. https://doi.org/10.1088/0034-4885/68/8/R06

Vasavada A et al (1998) Galileo imaging of Jupiter's atmosphere: the Great Red Spot, equatorial region, and white ovals. Icarus 135:265–275. https://doi.org/10.1006/icar.1998.5984

Wang B, Cai Z, Shen L, Liu T (2015) An analysis of physics-based optical flow method. J Comput Appl Maths 276:62–80. https://doi.org/10.1016/j.cam.2014.08.020

Willoughby HE, Clos JA, Shoreibah MG (1982) Concentric eye walls, secondary wind maxima, and the evolution of the hurricane vortex. J Atmos Sci 39:395–411. https://doi.org/10.1175/1520-0469(1982)039%3c0395:CEWSWM%3e2.0.CO;2

Willoughry HE, Darlling RW, Rahn ME (2006) Parametric representation of the primary hurricane vortex. Part II: a new family of sectionally continuous profiles. Mon Weather Rev 134:1102–1120. https://doi.org/10.1175/MWR3106.1

Wong MH, Marcus PS, Simon AA, Pater ID, Tollefson JW, Asay-Davis X (2021) Evolution of the horizontal winds in Jupiter's Great Red Spot from one Jovian year of HST/WFC3 maps. Geophys Res Lett 48(1):e2021GL093982. https://doi.org/10.1029/2021GL093982

Wu Q, Wang HQ, Lin YJ, Zhuang YZ, Zhang Y (2016) Deriving AMVs from geostationary satellite images using optical flow algorithm based on polynomial expansion. J Atmos Oceanic Technol 33(8):1727–1747. https://doi.org/10.1175/JTECH-D-16-0013.1